

Med-Scout: Curing MLLMs’ Geometric Blindness in Medical Perception via Geometry-Aware RL Post-Training

Anglin Liu¹ Ruichao Chen² Yi Lu¹ Hongxia Xu² Jintai Chen^{† 1,3}

Abstract

Despite recent Multimodal Large Language Models (MLLMs)’ linguistic prowess in medical diagnosis, we find even state-of-the-art MLLMs suffer from a critical perceptual deficit: **geometric blindness**. This failure to ground outputs in objective geometric constraints leads to plausible yet factually incorrect hallucinations, rooted in training paradigms that prioritize linguistic fluency over geometric fidelity. This paper introduces Med-Scout, a novel framework that “cures” this blindness via Reinforcement Learning (RL) that leverages the intrinsic geometric logic latent within unlabeled medical images. Instead of relying on costly expert annotations, Med-Scout derives verifiable supervision signals through three strategic proxy tasks: Hierarchical Scale Localization, Topological Jigsaw Reconstruction, and Anomaly Consistency Detection. To rigorously quantify this deficit, we present Med-Scout-Bench, a new benchmark specifically designed to evaluate geometric perception. Extensive evaluations show that Med-Scout significantly mitigates geometric blindness, outperforming leading proprietary and open-source MLLMs by over **40%** on our benchmark. Furthermore, this enhanced geometric perception generalizes to broader medical understanding, achieving superior results on radiological and comprehensive medical VQA tasks. The project page is: <https://c0216rc.github.io/Med-Scout/>.

1. Introduction

The deployment of Multimodal Large Language Models (MLLMs) in medical imaging necessitates a fundamental shift in priorities compared to general-domain vision-

¹The Hong Kong University of Science and Technology (Guangzhou) ²Zhejiang University ³The Hong Kong University of Science and Technology. Correspondence to: Jintai Chen <jintaiCHEN@hkust-gz.edu.cn>.

language tasks (Ye & Tang, 2025). While general-purpose models often prioritize open-ended creativity and linguistic fluency, medical visual perception demands an uncompromising adherence to objective geometric reality. A clinical AI system must not only interpret high-level semantic features but also rigorously respect the intrinsic geometric constraints of the image, such as relative anatomical scales, precise topology, and pixel-level structural consistency. However, despite the rapid evolution of both general (Liu et al., 2023; Bai et al., 2025b;a) and clinically adapted MLLMs (Chen et al., 2024; Team et al., 2025; Sellergren et al., 2025), a critical capability gap remains: while these models excel at generating semantically rich descriptions, they often suffer from **geometric blindness**, failing to ground their outputs in the strict geometric facts.

This misalignment stems largely from the limitations of prevailing training paradigms. Current approaches, including Supervised Fine-Tuning (SFT) and Reinforcement Learning (RL) (Murphy, 2024), predominantly optimize for semantic alignment, maximizing the likelihood of generating clinically plausible text conditioned on visual encodings. While effective for linguistic fluency, these objectives lack explicit mechanisms to penalize violations of physical laws. Consequently, models often generate professionally phrased reports that contradict the actual visual evidence, such as hallucinating lesions or misplacing organs. They essentially master complex medical terminology while failing to perceive the geometric reality of the scan accurately. Given the need for such strict geometric verification, RL methods (Schulman et al., 2017), specifically Group Relative Policy Optimization (GRPO) (Shao et al., 2024) presents an ideal optimization framework. Unlike standard supervision that relies on likelihood maximization, GRPO enables the model to learn directly from objective feedback signals. This mechanism is particularly effective for instilling geometric awareness, as it allows us to define and enforce explicit constraints that the model must satisfy.

Building upon this perspective, we introduce **Med-Scout**, a geometry-aware post-training framework designed to actively cure MLLMs’ geometric blindness in medical perception. Adopting a data-centric approach, we transform unlabeled medical images into objective supervision signals

by decomposing medical perception into three intrinsic geometric proxy tasks: (1) *Hierarchical Scale Localization*, enforcing awareness of anatomical details across varying scales; (2) *Topological Jigsaw Reconstruction*, demanding the understanding of global anatomical layouts; and (3) *Anomaly Consistency Detection*, necessitating comparative scrutiny to identify pixel-level structural artifacts. To drive the optimization of these tasks, we present a specialized Dense Geometric Reward (DGR) approach integrated within the GRPO framework, which provides dense, continuous guidance, effectively steering the geometric-semantic alignment to ensure stable and balanced convergence across the constructed task types. To support rigorous training and evaluation, we construct a comprehensive dataset comprising over 100K geometrically perturbed samples and curate a balanced 10% subset to establish Med-Scout-Bench, a novel benchmark that quantifies geometric blindness.

We apply Med-Scout to promote representative general-domain and medical-domain MLLMs. Experiments demonstrate that our approach not only significantly reduces geometric blindness on Med-Scout-Bench but also enables strong generalization to standard medical VQA (Lau et al., 2018; Liu et al., 2021; Zhang et al., 2023c; Hu et al., 2024; Zuo et al., 2025; Butsanets et al., 2025) and report generation tasks (Demner-Fushman et al., 2015; Johnson et al., 2019). This confirms that the geometric capabilities acquired through our post-training effectively transfer to broader medical perception.

Our main contributions are summarized as follows:

- *Unveiling Geometric Blindness.* We conduct a pilot study and identify a critical gap where MLLMs fail to ground outputs in geometric constraints despite semantic fluency.
- *Geometry-Aware RL Post-Training.* We propose Med-Scout, a novel RL framework that leverages specialized geometric proxy tasks to actively cure geometric blindness in MLLMs using dense geometric rewards.
- *The Med-Scout-Bench.* We release Med-Scout-Bench, a novel benchmark constructed from the intrinsic geometric properties of medical images. It serves as a rigorous standard for quantifying geometric perception, addressing a key evaluation gap.
- *Substantial Performance Improvements.* Med-Scout improves geometric perception by over **40%** on our benchmark and achieves state-of-the-art generalization on radiological and comprehensive medical VQA benchmarks.

2. Related Work

MLLMs for the Medical Domain. The advancement of medical visual understanding is currently driven by two com-

plementary paradigms. On one front, domain-specific adaptation has achieved remarkable precision through biomedical instruction tuning, as demonstrated by a growing array of specialized models (Li et al., 2023; Zhang et al., 2023a; Chen et al., 2024; Team et al., 2025; Pan et al., 2025). Simultaneously, general-purpose foundation models (Liu et al., 2023; Chen et al., 2023; Wang et al., 2025a; Bai et al., 2025a) have exhibited surprising zero-shot adaptability to radiological tasks, benefiting from massive-scale pre-training (Zhang et al., 2023b) and robust visual representations. However, despite these distinct strengths, both paradigms share a critical vulnerability: they frequently prioritize linguistic fluency over physical grounding. This results in pervasive “geometric blindness,” where models successfully describe pathologies but fail to adhere to the strict spatial constraints and anatomical layouts inherent in medical images.

Enhance MLLM with Proxy Tasks. Recent advancements have integrated verifiable proxy tasks into RL to enhance visual grounding. Jigsaw-R1 (Wang et al., 2025c) and Visual Jigsaw (Wu et al., 2025) established that grid reconstruction significantly improves fine-grained perception, and formalize such objective tasks into RL pipelines. ViCrit (Wang et al., 2025b) employs executable programs for robust verification. Approaches like Euclid (Zhang et al., 2024), GeoPQA (Chen et al., 2025), and GeoGPT4V (Cai et al., 2024) attempt to augment MLLMs with geometric priors, but their task formulations remain incompatible with the unique requirements of medical perception. All these methods fail to address comprehensive clinical constraints like multi-scale consistency and anomaly focus. Moreover, their reliance on sparse binary feedback lacks the granularity essential for complex medical reasoning.

3. Pilot Study

We conducted three preliminary experiments on Qwen3-VL-8B-Instruct (Bai et al., 2025a) and Lingshu-7B (Team et al., 2025) to investigate the geometric fidelity of MLLMs, as shown in Figure 1. Our three findings are summarized as follows:

3.1. Finding I: Inconsistency Between Different Scales

We investigated whether models can consistently integrate visual features across scales. We specifically filtered for 200 positive samples where the models correctly identified lesions in cropped local views. We then evaluated the models on the corresponding original global images of these successfully recognized crops.

Result: Models failed to detect the same lesions in over 20% of the global views. This performance drop indicates the models struggle to preserve visual perception when the spatial scale changes.

3.2. Finding II: Blindness to Relative Spatial Positions

We tested whether models verify actual relative spatial positions or rely on semantic priors. We selected 200 images with correctly identified pathology locations and rotated them by 180 degrees. In this inverted view, anatomically “upper” structures appear at the visual bottom.

Result: Models failed to adapt their spatial descriptions in 80% of cases. This performance drop indicates the models rely on rigid priors rather than reasoning about the actual topological positions.

3.3. Finding III: Insensitivity to Structural Anomalies

We examined sensitivity to pixel-level structural consistency using a “cut-paste” protocol. We artificially replaced image patches with structurally incoherent blocks in 200 samples and prompted models to describe findings.

Result: Models failed to identify the artifacts in over 90% of cases. Rather than identifying the artifact, they produced standard reports that entirely overlooked the artificial perturbations. This indicates the models’ blindness to abnormal geometric manifestations.

3.4. Summary

These experiments reveal critical blindness of current MLLMs: (1) inability to transfer recognition between different scales; (2) blindness to real topological positions; and (3) insensitivity to structural inconsistencies. This semantic-geometric misalignment directly motivates our proposed

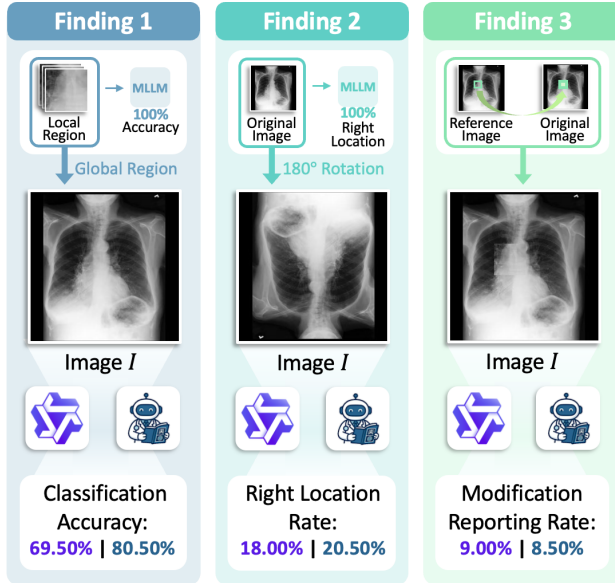


Figure 1. Pilot Study: (Left) Scale Blindness: The model correctly describes findings in a local crop but fails in the full global view. (Middle) Topology Blindness: When the image is rotated, the model fails to update location descriptions. (Right) Anomaly Blindness: The model completely overlooks obvious artificial modifications.

Med-Scout framework to actively cure these blind spots, thereby grounding semantic generation in geometric reality.

4. Med-Scout

4.1. Task Formulation

We formulate Med-Scout as a geometry-aware RL post-training process, as shown in Figure 2. Our goal is to transform unlabeled medical images into three verifiable geometric proxy tasks $\mathcal{T} = \{\mathcal{T}_{\text{scale}}, \mathcal{T}_{\text{topo}}, \mathcal{T}_{\text{anom}}\}$ as shown in Appendix A.2. Formally, given a raw medical image $I \in \mathbb{R}^{H \times W}$, we generate a VQA case.

Task A: Hierarchical Scale Localization ($\mathcal{T}_{\text{scale}}$).

Construction: To enforce multi-scale processing under high cognitive load, we simultaneously crop $N = 3$ local patches from the original image I . These patches are sampled from two distinct scale levels: Level 1 (20% of image area) and Level 2 (6.25% of image area). To filter out non-informative background noise, the center coordinates are strictly restricted to the central normalized region (within the $[0.2, 0.8]$ range).

Objective: The model identifies the scale level and predicts the normalized bounding box $b = (x_1, y_1, x_2, y_2)$ for each of the N patches. This compels the model to maintain multiple coordinate contexts and master absolute spatial grounding.

Task B: Topological Jigsaw Reconstruction ($\mathcal{T}_{\text{topo}}$).

Construction: We partition the image I into a 2×2 grid and apply a random permutation σ to generate a shuffled observation I_{shuffled} , retaining sufficient foreground semantic content while requiring both horizontal and vertical spatial reasoning.

Objective: The model must reconstruct the sequence of original indices corresponding to the shuffled positions (reading left-to-right, top-to-bottom). This task forces the model to deduce the canonical global layout of anatomical structures through logical geometric deduction.

Task C: Anomaly Consistency Detection ($\mathcal{T}_{\text{anom}}$).

Construction: We employ a fine-grained “cut-paste” strategy on a 4×4 grid. We specifically target the core anatomical region by replacing one patch within the central indices with a reference patch from I_{ref} . To ensure realism, I_{ref} is selected via modality-specific protocols: adjacent slices for volumetric data (CT/ MRI) or the top-1 most similar image retrieved via BiomedCLIP (Zhang et al., 2023b) for X-ray.

Objective: The model outputs the grid index of the inconsistent patch. By focusing on the high-density central region with a fine granularity, this task necessitates comparative reasoning to detect subtle pixel-level discontinuities that

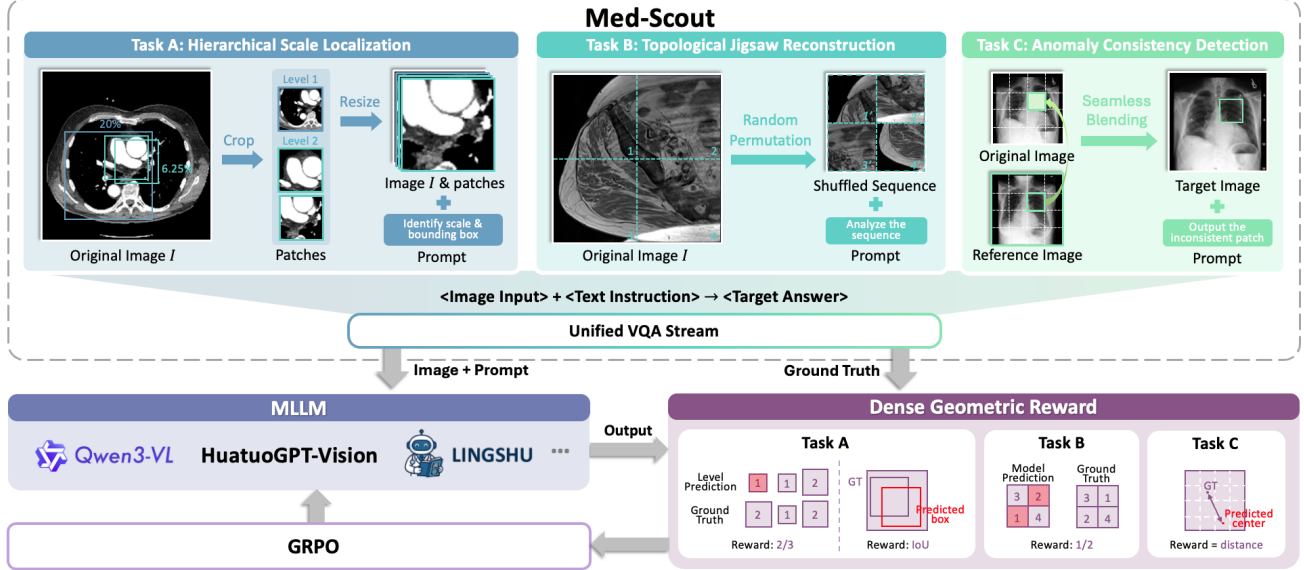


Figure 2. Overview of the Med-Scout Framework. We transform unlabeled medical images into three proxy tasks to cure geometric blindness actively. The framework is optimized using GRPO with a Dense Geometric Reward mechanism that provides stable feedback.

violate anatomical coherence.

Unified VQA Stream & Optimization. We unify these tasks into a standard open-set VQA format as shown in Appendix A.3 and require the model to generate precise answers:

- **Direct Mode:** The model directly generates the final answer.
- **Reasoning Mode:** The model generates a Chain-of-Thought (CoT) (Wei et al., 2022) reasoning path followed by the answer, allowing it to articulate geometric constraints before concluding.

The final training objective is to maximize the expected reward \mathcal{R} across these generative tasks.

4.2. Reward Formulation

To overcome the sparsity of binary feedback in traditional RL, we design a dense geometric reward mechanism. Instead of a simple pass/fail metric, our system calculates continuous reward values based on the degree of geometric deviation, encouraging progressive refinement. The total reward \mathcal{R} is composed of three components:

$$\mathcal{R} = \mathcal{R}_{\text{acc}} + \mathcal{R}_{\text{fmt}} + \mathbb{I}_{\text{CoT}} \cdot \mathcal{R}_{\text{reason}} \quad (1)$$

where $\mathcal{R}_{\text{acc}} \in [0, 1]$ measures task accuracy, $\mathcal{R}_{\text{fmt}} \in [0, 0.5]$ ensures output format compliance, and $\mathcal{R}_{\text{reason}} \in [0, 0.5]$ enforces reasoning structure in CoT mode.

Dense Geometric Rewards (\mathcal{R}_{acc}). We tailor specific continuous metrics for each task type to quantify geometric precision, capped at a maximum of 1.0.

- **Scale ($\mathcal{T}_{\text{scale}}$):** This task entails quantifying attributes and localizing targets for N objects simultaneously. We evaluate performance across two dimensions, normalizing by N to ensure invariant optimization magnitude:

1. *Value Estimation:* For discrete scale levels, we compute the average classification correctness. For a target index sequence Y^* of length N :

$$\mathcal{R}_{\text{val}} = \frac{1}{N} \sum_{i=1}^N \mathbb{I}(\hat{y}_i = y_i^*) \quad (2)$$

2. *Box Localization:* To enforce spatial precision, we calculate the average Intersection over Union (IoU) between the predicted box \hat{b}_i and the ground truth b_i^* :

$$\mathcal{R}_{\text{box}} = \frac{1}{N} \sum_{i=1}^N \text{IoU}(\hat{b}_i, b_i^*) \quad (3)$$

- **Topology ($\mathcal{T}_{\text{topo}}$):** To reward partial logical correctness, we utilize an element-wise alignment metric rather than exact sequence matching. For a target index sequence S^* of length N :

$$\mathcal{R}_{\text{topo}} = \frac{1}{N} \sum_{i=1}^N \mathbb{I}(\hat{s}_i = s_i^*) \quad (4)$$

This ensures the model receives credit for every correctly positioned patch, even if the global sequence is imperfect.

- **Anomaly ($\mathcal{T}_{\text{anom}}$):** The objective is to identify the single swapped patch index $k \in \{0, \dots, 15\}$ within a 4×4 grid. To provide dense supervision, we first map the flattened

index k to 2D grid coordinates (u, v) via $u = \lfloor k/4 \rfloor$ and $v = k \pmod 4$. We then compute the reward based on the Euclidean distance between the predicted patch coordinates (\hat{u}, \hat{v}) and the ground truth (u^*, v^*) :

$$\mathcal{R}_{\text{anom}} = \exp \left(-\frac{\sqrt{(\hat{u} - u^*)^2 + (\hat{v} - v^*)^2}}{\tau} \right) \quad (5)$$

where τ is a temperature hyperparameter. This distance-based mechanism guides the model towards the correct spatial region, rewarding predictions that are geometrically plausible even if the exact index is missed.

Universal Format Reward (\mathcal{R}_{fmt}). To strictly enforce output protocols, we evaluate format compliance at the item level rather than the sequence level. Given a target answer containing N required elements, the reward is calculated as:

$$\mathcal{R}_{\text{fmt}} = \frac{0.5}{N} \sum_{i=1}^N \mathbb{I}(\hat{a}_i \in \Phi_{\text{regex}}) \quad (6)$$

where Φ_{regex} represents the valid pattern for each sub-component.

Reasoning Structure Reward ($\mathcal{R}_{\text{reason}}$). Exclusively in Reasoning Mode, we impose an additional structural constraint to enforce the CoT pattern `<think>...<answer>....`. This encourages the model to maintain the reasoning buffer:

$$\mathcal{R}_{\text{reason}} = \begin{cases} 0.5 & \text{if } \hat{Y} \in \Phi_{\text{CoT}} \\ 0 & \text{otherwise} \end{cases} \quad (7)$$

Consequently, a perfectly reasoned and accurate response in CoT mode yields a maximum total reward of $\mathcal{R} = 2.0$.

4.3. Med-Scout-Bench

To quantitatively evaluate geometric blindness, we introduce Med-Scout-Bench, a novel benchmark encompassing diverse anatomical regions from the mainstream radiological modalities (CT, MRI, and X-ray), pivotal for clinical geometric analysis.

Dataset Construction. We synthesize an initial pool of 108,000 VQA cases. We utilize *TotalSegmentor* (CT/MRI) (Wasserthal et al., 2023; Akinci D’Antonoli et al., 2025) to guarantee comprehensive anatomical coverage across the entire body, alongside *MIMIC-CXR* (Johnson et al., 2019) for planar radiography. From this pool, we sampled a high-quality subset of 10,800 cases (10%) as the benchmark. This benchmark is strictly balanced across the three radiological modalities, ensuring unbiased evaluation.

Evaluation Protocol. We adopt a unified evaluation setting to ensure consistency: all tasks are formulated as open-set

VQA queries rather than multiple-choice options. We employ the LLM-as-a-Judge (Gu et al., 2024) paradigm to robustly assess the semantic correctness of these generative responses, overcoming the limitations of rigid string matching.

5. Experiments

5.1. Experimental Settings

Med-Scout Training. All Med-Scout experiments are conducted for 7,200 steps on a node with $6 \times$ NVIDIA RTX PRO 6000 GPUs using GRPO. We optimize the model using AdamW with a peak learning rate of 1×10^{-6} , a cosine decay schedule, and a warm-up ratio of 0.01. For the GRPO configuration, we set the global batch size to 192 and the group size to $G = 8$, with a KL divergence coefficient $\beta = 0.04$ to ensure stable updates. Training is performed on the 97,200-sample split of our constructed dataset excluding the Med-Scout-Bench. We adopt the LLM-as-a-Judge paradigm using Gemini-3-Flash to evaluate open-ended responses rigorously.

Baselines. To assess the generalizability of our framework across different model scales and domains, we apply Med-Scout to four backbones: the general-purpose Qwen3-VL-4B/8B-Instruct (Bai et al., 2025a) and the medical specialists Lingshu-7B (Team et al., 2025) and HuatuoGPT-Vision-7B (Chen et al., 2024). We benchmark our approach against a wide range of state-of-the-art (SOTA) MLLMs, including both proprietary and open-source models.

- **Proprietary Models:** We evaluate the latest commercial leaders, GPT-5 and Gemini-3-Flash, to establish upper-bound performance benchmarks.
- **General-purpose MLLMs:** We select representative open-source models including InternVL3-8B (Zhu et al., 2025), Qwen2.5-VL-3B-Instruct, Qwen2.5-VL-7B-Instruct (Bai et al., 2025b), as well as the newer Qwen3-VL-4B-Instruct and Qwen3-VL-8B-Instruct (Bai et al., 2025a).
- **Medical MLLMs:** For domain-specific comparison, we utilize LLaVA-Med-7B (Li et al., 2023), MedGemma-4B-IT (Sellergren et al., 2025), HuatuoGPT-Vision-7B (Chen et al., 2024), and Lingshu-7B (Team et al., 2025).

To ensure evaluation fairness, all models are assessed within the same standardized evaluation environment.

Benchmarks. We conduct comprehensive evaluations across three dataset categories. First, to quantify geometric perception, we utilize our Med-Scout-Bench. Second, we assess standard radiological VQA using RadImageNet-VQA (Butsanets et al., 2025), VQA-RAD (Lau et al., 2018),

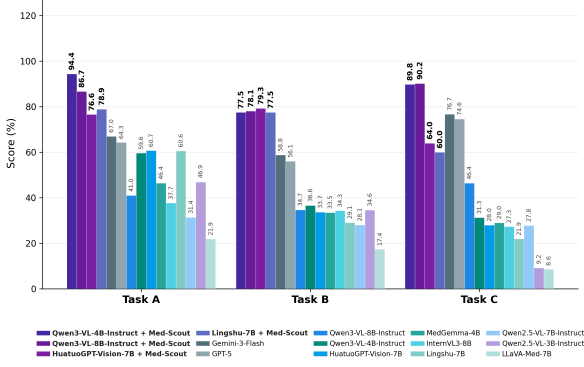


Figure 3. Performance comparison on Med-Scout-Bench.

and SLAKE (Liu et al., 2021), alongside MIMIC-CXR and IU-Xray for report generation. Finally, to verify broad generalization, we extend our evaluation to PMC-VQA (Zhang et al., 2023c), OmniMedVQA (Hu et al., 2024), and MedXpertQA (Hu et al., 2024) for broader medical domains and diverse modalities.

Evaluation Metrics. For Med-Scout-Bench, we report the DGR score computed directly via the reward functions defined in Section 4.2. For VQA benchmarks, we report the response accuracy. For report generation tasks, we report metrics including ROUGE-L (Lin, 2004), CIDEr (Vedantam et al., 2015), and SemScore (Ayneddinov & Akbik, 2024) for both semantic-based and model-based evaluation.

5.2. Results on Med-Scout-Bench

As shown in Figure 3 and Table 5, Med-Scout yields substantial improvements across all backbones. For instance, the aligned Qwen3-VL-8B-Instruct improves average accuracy from 39.7% to 83.6%, while Lingshu-7B rises from 31.9% to 71.9%. Notably, open-source models outperform leading proprietary models GPT-5 and Gemini-3-Flash. Moreover, general-domain models show greater improvement than medical specialists, suggesting that a strong vision-language foundation enables models to learn geometric features more effectively.

5.3. Results on Radiological VQA Benchmarks

Tables 1 and 2 present the evaluation results on radiological VQA and report generation benchmarks, respectively. Med-Scout consistently enhances performance across both discriminative and generative tasks. In VQA, Qwen3-VL-4B achieves a notable 4.2% gain on Rad-VQA, while our aligned Lingshu-7B surpasses Gemini-3-Flash on VQA-RAD (71.0% vs. 70.2%).

The benefits of geometric alignment are even more pronounced in report generation tasks, where geometric accuracy is critical. As shown in Table 2, Med-Scout boosts Qwen3-VL-4B's CIDEr score by 4.3% on MIMIC-CXR.

Most remarkably, Lingshu-7B with Med-Scout achieves an SOTA CIDEr, dramatically outperforming proprietary models. This confirms that curing geometric blindness enables models to generate clinically accurate reports with superior geometric consistency.

5.4. Generalization to Comprehensive Medical VQA Benchmarks

We further extend our evaluation to broader medical domains using PMC-VQA, OmniMedVQA, and MedXpertQA. As shown in Table 1, Med-Scout confers consistent improvements, demonstrating that geometric awareness is fundamental to general medical perception. Notably, HuatuGPT-Vision-7B achieves a substantial 2.9% gain on PMC-VQA. Even more impressively, Lingshu-7B manages to break through its performance ceiling, further elevating its already SOTA results. This confirms that our framework effectively enhances robustness in complex, open-domain medical perception.

5.5. Direct Mode vs. Reasoning Mode

As illustrated in Figure 4, the negligible performance gap between Direct Mode (+M) and Reasoning Mode (+M (R)) suggests that explicit CoT is not strictly necessary. However, this similarity may partially stem from our reasoning structure reward (R_{reason}) prioritizing structural constraints over logical validity.

5.6. Data Scaling Analysis

To evaluate the scalability and data efficiency of our framework, we conducted a quantitative analysis across varying training set sizes.

Med-Scout-Bench Scalability. As shown in Figure 5 (Left), performance on Med-Scout-Bench improves consistently

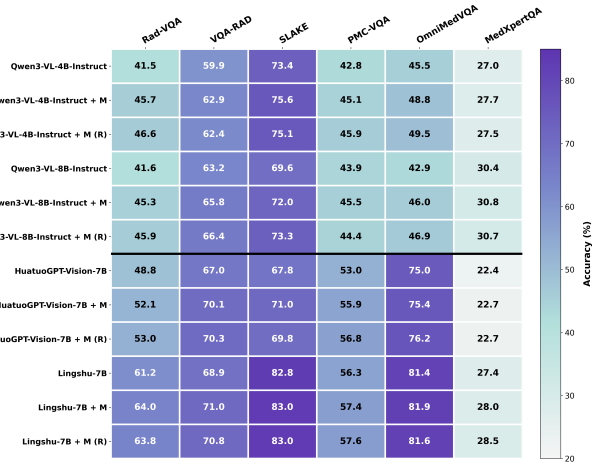


Figure 4. Performance comparison on six public benchmarks. Purple colors correspond to higher accuracy. Direct Mode (+M) and Reasoning Mode (+M (R)) show close performance.

Table 1. Performance comparison with SOTA MLLMs across radiological and general medical VQA benchmarks. Rad-VQA represents RadImageNet-VQA. All accuracy metrics are scaled by a factor of 100 to enhance clarity and comprehension. The best results are highlighted.

MODEL	RADIOLOGICAL VQA			GENERALIZATION		
	RAD-VQA	VQA-RAD	SLAKE	PMC-VQA	OMNIMEDVQA	MEDXPERTVQA
<i>Proprietary Models</i>						
GPT-5	59.1	66.4	73.9	57.7	76.9	54.8
GEMINI-3-FLASH	60.7	70.2	76.1	58.1	75.3	56.0
<i>General-purpose MLLMs</i>						
INTERNVL3-8B	58.4	65.6	72.9	52.0	78.2	22.4
QWEN2.5-VL-3B-INSTRUCT	54.1	60.2	63.5	50.2	61.5	24.3
QWEN2.5-VL-7B-INSTRUCT	55.7	65.3	67.9	51.8	63.8	21.9
QWEN3-VL-4B-INSTRUCT	41.5	59.9	73.4	42.8	45.5	27.0
+ MED-SCOUT	45.7↑4.2	62.9↑3.0	75.6↑2.2	45.1↑2.3	48.8↑3.3	27.7↑0.7
QWEN3-VL-8B-INSTRUCT	41.6	63.2	69.6	43.9	42.9	30.4
+ MED-SCOUT	45.3↑3.7	65.8↑2.6	72.0↑2.4	45.5↑1.6	46.0↑3.1	30.8↑0.4
<i>Medical MLLMs</i>						
LLAVA-MED-7B	44.3	50.6	50.1	32.4	46.8	19.9
MEDGEMMA-4B-IT	49.8	70.8	77.9	48.7	70.3	22.0
HUATUOGPT-VISION-7B	48.8	67.0	67.8	53.0	75.0	22.4
+ MED-SCOUT	52.1↑3.3	70.1↑3.1	71.0↑3.2	55.9↑2.9	75.4↑0.4	22.7↑0.3
LINGSHU-7B	61.2	68.9	82.8	56.3	81.4	27.4
+ MED-SCOUT	64.0↑2.8	71.0↑2.1	83.0↑0.2	57.4↑1.1	81.9↑0.5	28.0↑0.6

across all backbone models as the training data volume increases from 20% to 100%. The substantial performance gain in the early stages underscores the high efficiency and quality of our automatically generated supervision signals, while the continuous upward trend without saturation suggests the models have not yet reached their capacity limits.

Generalization Correlation. Figure 5 (Right) reveals a strong positive correlation between internal alignment scores and performance on six external benchmarks. This confirms that improving geometric awareness enhances general medical perception. Consequently, Med-Scout-Bench serves as a reliable indicator of broader clinical visual reasoning capabilities.

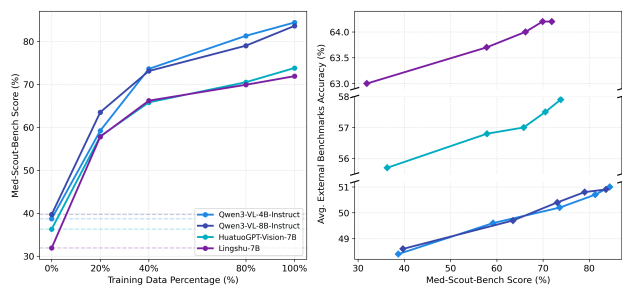


Figure 5. Data Scaling and Generalization Analysis. Left: Continuous performance improvement on Med-Scout-Bench with increasing training data. Right: Strong positive correlation between Med-Scout-Bench scores and average accuracy on external benchmarks.

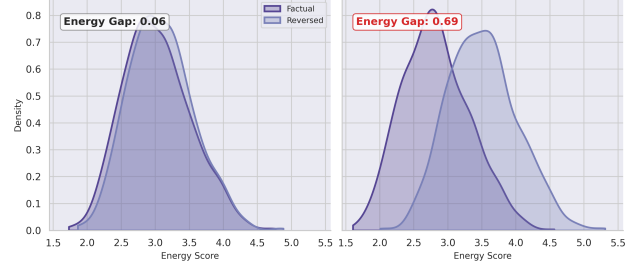


Figure 6. Energy Landscape of Factual Consistency. We visualize energy distributions for 800 factual (purple) versus spatially inverted (blue) report pairs. Left: Qwen3-VL-4B-Instruct exhibits overlapping distributions. Right: Qwen3-VL-4B-Instruct with Med-Scout establishes a distinct energy barrier.

5.7. Extensive Analysis

We conducted an extensive analysis to evaluate the impact of Med-Scout on the spatial discrimination capabilities of MLLMs and their visual attention focus on target regions.

Energy Landscape of Factual Consistency. Following the Energy-Based model (Song & Kingma, 2021), we quantify the compatibility between visual evidence x and textual description y via the energy function $E(x, y) = -\log P_\theta(y|x)$, implemented as the negative log-likelihood of the target response. To evaluate this, we constructed a probe dataset of 800 factual-counterfactual pairs from MIMIC-CXR by inverting anomaly-related spatial locatives in ground-truth chest X-ray reports. As visualized in Figure 6, the Qwen3-VL-4B-Instruct model exhibits a collapsed landscape where factual and perturbed descriptions share

Table 2. Performance comparison on medical report generation benchmarks. Results are reported on ROUGE-L, CIDEr, and SemScore metrics. All scores are scaled by a factor of 100 to enhance clarity and comprehension. The best results are highlighted.

MODEL	MIMIC-CXR			IU-XRAY		
	ROUGE-L	CIDEr	SEMScore	ROUGE-L	CIDEr	SEMScore
<i>Proprietary Models</i>						
GPT-5	14.7	89.4	25.2	34.6	139.9	48.3
GEMINI-3-FLASH	24.9	90.0	29.8	35.1	135.8	48.0
<i>General-purpose MLLMs</i>						
INTERNL3-8B	20.7	64.3	21.1	22.4	70.2	30.6
QWEN2.5-VL-3B-INSTRUCT	21.4	57.7	19.4	26.7	72.9	37.2
QWEN2.5-VL-7B-INSTRUCT	22.9	63.9	18.6	26.6	78.8	36.3
QWEN3-VL-4B-INSTRUCT	21.8	60.9	19.8	25.8	81.4	36.5
+ MED-SCOUT	23.4↑1.6	65.2↑4.3	21.5↑1.7	27.1↑1.3	84.2↑2.8	38.6↑2.1
QWEN3-VL-8B-INSTRUCT	21.3	64.8	19.6	27.1	75.9	38.7
+ MED-SCOUT	23.8↑2.5	68.1↑3.3	21.0↑1.4	29.5↑2.4	79.6↑3.7	41.6↑2.9
<i>Medical MLLMs</i>						
LLAVA-MED-7B	16.4	49.2	16.7	19.5	73.7	17.4
MEDGEMMA-4B-IT	27.4	83.8	30.1	30.6	107.5	46.8
HUATUOGPT-VISION-7B	23.6	75.6	24.6	30.9	109.6	40.7
+ MED-SCOUT	25.7↑2.1	79.0↑3.4	25.8↑1.2	32.1↑1.2	111.7↑2.1	43.1↑2.4
LINGSHU-7B	30.9	104.9	29.7	37.7	180.8	48.4
+ MED-SCOUT	31.4↑0.5	105.2↑0.3	30.3↑0.6	38.0↑0.3	183.3↑2.5	48.6↑0.2

overlapping energy distributions ($\text{Gap} \approx 0.06$), indicating geometric blindness. In contrast, Med-Scout establishes a distinct energy barrier ($\text{Gap} \approx 0.69$), effectively assigning high-energy states to spatial hallucinations while preserving low energy for factual descriptions. This separation suggests that Med-Scout has successfully internalized the spatial constraints of medical imagery, moving beyond mere language priors to achieve rigorous geometric alignment.

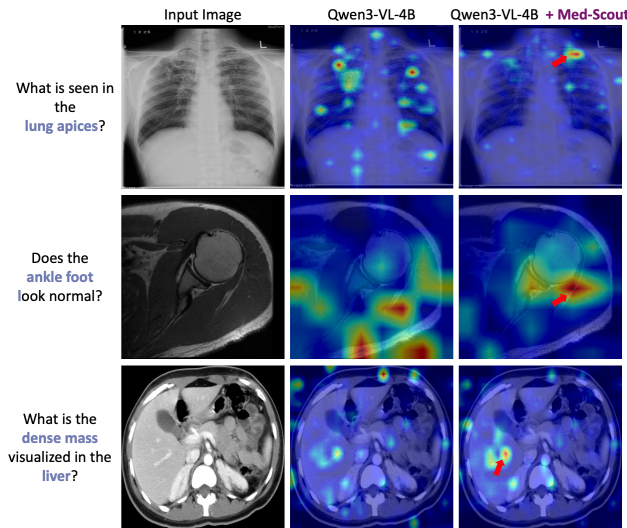


Figure 7. Visualization of attention maps on critical anatomical regions. We compare the visual attention of the baseline Qwen3-VL-4B-Instruct (Middle) versus the model aligned with Med-Scout (Right) given specific anatomical queries. While the baseline model exhibits scattered attention and frequently drifts to irrelevant background noise, Med-Scout demonstrates a highly concentrated focus on the critical target regions.

Analysis of Attention on Critical Region. We followed (Zhang et al., 2025) and visualized the attention maps of the MLLM on specific anatomical queries (Figure 7). The baseline model exhibits scattered attention and frequently drifts to irrelevant background noise. In contrast, Med-Scout demonstrates a highly concentrated focus on the critical regions, such as *lung apices*, *ankle joints*, or *dense mass in liver*. This shift confirms that our challenging geometric proxy tasks motivate the model to transition from superficial scanning to fine-grained visual scrutiny, thus effectively enhancing the model’s sensitivity to local visual evidence. This improved grounding not only translates directly to the external benchmarks’ performance but also provides the reliability essential for medical understanding.

6. Conclusion

Motivated by a pilot study revealing the significant “geometric blindness” of MLLMs in medical perception, this paper proposes Med-Scout and Med-Scout-Bench, a geometry-aware RL post-training framework designed to cure this blindness and a novel benchmark aimed to quantify this limitation rigorously. By aligning semantic generation with geometric reality through three intrinsic proxy tasks and a dense reward mechanism that stabilizes the optimization process, Med-Scout significantly enhances the geometric perception of existing MLLMs and further improves performance on radiological and comprehensive medical VQA benchmarks. Moreover, further analysis reveals the potential of this strategy in maintaining the geometric truth of medical images, thereby substantially enhancing visual capabilities.

References

Akinci D'Antonoli, T., Berger, L. K., Indrakanti, A. K., Vishwanathan, N., Weiss, J., Jung, M., Berkarda, Z., Rau, A., Reisert, M., Küstner, T., et al. Totalsegmentator mri: Robust sequence-independent segmentation of multiple anatomic structures in mri. *Radiology*, 314(2):e241613, 2025.

Aynedtinov, A. and Akbik, A. Semscore: Automated evaluation of instruction-tuned LLMs based on semantic textual similarity. *CoRR*, abs/2401.17072, 2024. doi: 10.48550/ARXIV.2401.17072. URL <https://doi.org/10.48550/arXiv.2401.17072>.

Bai, S., Cai, Y., Chen, R., Chen, K., Chen, X., Cheng, Z., Deng, L., Ding, W., Gao, C., Ge, C., Ge, W., Guo, Z., Huang, Q., Huang, J., Huang, F., Hui, B., Jiang, S., Li, Z., Li, M., Li, M., Li, K., Lin, Z., Lin, J., Liu, X., Liu, J., Liu, C., Liu, Y., Liu, D., Liu, S., Lu, D., Luo, R., Lv, C., Men, R., Meng, L., Ren, X., Ren, X., Song, S., Sun, Y., Tang, J., Tu, J., Wan, J., Wang, P., Wang, P., Wang, Q., Wang, Y., Xie, T., Xu, Y., Xu, H., Xu, J., Yang, Z., Yang, M., Yang, J., Yang, A., Yu, B., Zhang, F., Zhang, H., Zhang, X., Zheng, B., Zhong, H., Zhou, J., Zhou, F., Zhou, J., Zhu, Y., and Zhu, K. Qwen3-VL technical report. *CoRR*, abs/2511.21631, 2025a. doi: 10.48550/ARXIV.2511.21631. URL <https://doi.org/10.48550/arXiv.2511.21631>.

Bai, S., Chen, K., Liu, X., Wang, J., Ge, W., Song, S., Dang, K., Wang, P., Wang, S., Tang, J., Zhong, H., Zhu, Y., Yang, M., Li, Z., Wan, J., Wang, P., Ding, W., Fu, Z., Xu, Y., Ye, J., Zhang, X., Xie, T., Cheng, Z., Zhang, H., Yang, Z., Xu, H., and Lin, J. Qwen2.5-VL technical report. *CoRR*, abs/2502.13923, 2025b. doi: 10.48550/ARXIV.2502.13923. URL <https://doi.org/10.48550/arXiv.2502.13923>.

Butsanets, L., Corbière, C., Khlaut, J., Manceron, P., and Dancette, C. RadImageNet-VQA: A large-scale CT and MRI dataset for radiologic visual question answering, 2025. URL <https://arxiv.org/abs/2512.17396>.

Cai, S., Bao, K., Guo, H., Zhang, J., Song, J., and Zheng, B. Geogpt4v: Towards geometric multi-modal large language models with geometric image generation. In Al-Onaizan, Y., Bansal, M., and Chen, Y. (eds.), *Proceedings of the 2024 Conference on Empirical Methods in Natural Language Processing, EMNLP 2024, Miami, FL, USA, November 12-16, 2024*, pp. 750–766. Association for Computational Linguistics, 2024. doi: 10.18653/V1/2024.EMNLP-MAIN.44. URL <https://doi.org/10.18653/v1/2024.emnlp-main.44>.

Chen, G., Xu, W., Zhang, H., Chan, H. P., Zhao, D., Luu, A. T., and Rong, Y. Geopqa: Bridging the visual perception gap in MLLMs for geometric reasoning. *CoRR*, abs/2509.17437, 2025. doi: 10.48550/ARXIV.2509.17437. URL <https://doi.org/10.48550/arXiv.2509.17437>.

Chen, J., Ouyang, R., Gao, A., Chen, S., Chen, G. H., Wang, X., Zhang, R., Cai, Z., Ji, K., Yu, G., Wan, X., and Wang, B. HuatuoGPT-Vision, towards injecting medical visual knowledge into multimodal LLMs at scale. *CoRR*, abs/2406.19280, 2024. doi: 10.48550/ARXIV.2406.19280. URL <https://doi.org/10.48550/arXiv.2406.19280>.

Chen, Z., Wu, J., Wang, W., Su, W., Chen, G., Xing, S., Zhong, M., Zhang, Q., Zhu, X., Lu, L., Li, B., Luo, P., Lu, T., Qiao, Y., and Dai, J. InternVL: Scaling up vision foundation models and aligning for generic visual-linguistic tasks. *CoRR*, abs/2312.14238, 2023. doi: 10.48550/ARXIV.2312.14238. URL <https://doi.org/10.48550/arXiv.2312.14238>.

DeepSeek-AI, Liu, A., Mei, A., Lin, B., Xue, B., Wang, B., Xu, B., Wu, B., Zhang, B., Lin, C., Dong, C., Lu, C., Zhao, C., Deng, C., Xu, C., Ruan, C., Dai, D., Guo, D., Yang, D., Chen, D., Li, E., Zhou, F., Lin, F., Dai, F., Hao, G., Chen, G., Li, G., Zhang, H., Xu, H., Li, H., Liang, H., Wei, H., Zhang, H., Luo, H., Ji, H., Ding, H., Tang, H., Cao, H., Gao, H., Qu, H., Zeng, H., Huang, J., Li, J., Xu, J., Hu, J., Chen, J., Xiang, J., Yuan, J., Cheng, J., Zhu, J., Ran, J., Jiang, J., Qiu, J., Li, J., Song, J., Dong, K., Gao, K., Guan, K., Huang, K., Zhou, K., Huang, K., Yu, K., Wang, L., Zhang, L., Wang, L., Zhao, L., Yin, L., Guo, L., Luo, L., Ma, L., Wang, L., Zhang, L., Di, M. S., Xu, M. Y., Zhang, M., Zhang, M., Tang, M., Zhou, M., Huang, P., Cong, P., Wang, P., Wang, Q., Zhu, Q., Li, Q., Chen, Q., Du, Q., Xu, R., Ge, R., Zhang, R., Pan, R., Wang, R., Yin, R., Xu, R., Shen, R., Zhang, R., Liu, S. H., Lu, S., Zhou, S., Chen, S., Cai, S., Chen, S., Hu, S., Liu, S., Hu, S., Ma, S., Wang, S., Yu, S., Zhou, S., Pan, S., Zhou, S., Ni, T., Yun, T., Pei, T., Ye, T., Yue, T., Zeng, W., Liu, W., Liang, W., Pang, W., Luo, W., Gao, W., Zhang, W., Gao, X., Wang, X., Bi, X., Liu, X., Wang, X., Chen, X., Zhang, X., Nie, X., Cheng, X., Liu, X., Xie, X., Liu, X., Yu, X., Li, X., Yang, X., Li, X., Chen, X., Su, X., Pan, X., Lin, X., Fu, X., Wang, Y. Q., Zhang, Y., Xu, Y., Ma, Y., Li, Y., Li, Y., Zhao, Y., Sun, Y., Wang, Y., Qian, Y., Yu, Y., Zhang, Y., Ding, Y., Shi, Y., Xiong, Y., He, Y., Zhou, Y., Zhong, Y., Piao, Y., Wang, Y., Chen, Y., Tan, Y., Wei, Y., Ma, Y., Liu, Y., Yang, Y., Guo, Y., Wu, Y., Wu, Y., Cheng, Y., Ou, Y., Xu, Y., Wang, Y., Gong, Y., Wu, Y., Zou, Y., Li, Y., Xiong, Y., Luo, Y., You, Y., Liu, Y., Zhou, Y., Wu, Z. F., Ren, Z. Z., Zhao, Z., Ren, Z., Sha, Z., Fu, Z., Xu, Z., Xie, Z., Zhang, Z., Hao, Z.,

Gou, Z., Ma, Z., Yan, Z., Shao, Z., Huang, Z., Wu, Z., Li, Z., Zhang, Z., Xu, Z., Wang, Z., Gu, Z., Zhu, Z., Li, Z., Zhang, Z., Xie, Z., Gao, Z., Pan, Z., Yao, Z., Feng, B., Li, H., Cai, J. L., Ni, J., Xu, L., Li, M., Tian, N., Chen, R. J., Jin, R. L., Li, S. S., Zhou, S., Sun, T., Li, X. Q., Jin, X., Shen, X., Chen, X., Song, X., Zhou, X., Zhu, Y. X., Huang, Y., Li, Y., Zheng, Y., Zhu, Y., Ma, Y., Huang, Z., Xu, Z., Zhang, Z., Ji, D., Liang, J., Guo, J., Chen, J., Xia, L., Wang, M., Li, M., Zhang, P., Chen, R., Sun, S., Wu, S., Ye, S., Wang, T., Xiao, W. L., An, W., Wang, X., Sun, X., Wang, X., Tang, Y., Zha, Y., Zhang, Z., Ju, Z., Zhang, Z., and Qu, Z. Deepseek-v3.2: Pushing the frontier of open large language models, 2025. URL <https://arxiv.org/abs/2512.02556>.

Demner-Fushman, D., Kohli, M. D., Rosenman, M. B., Shooshan, S. E., Rodriguez, L., Antani, S., Thoma, G. R., and McDonald, C. J. Preparing a collection of radiology examinations for distribution and retrieval. *Journal of the American Medical Informatics Association*, 23(2):304–310, 2015.

Gu, J., Jiang, X., Shi, Z., Tan, H., Zhai, X., Xu, C., Li, W., Shen, Y., Ma, S., Liu, H., Wang, Y., and Guo, J. A survey on llm-as-a-judge. *CoRR*, abs/2411.15594, 2024. doi: 10.48550/ARXIV.2411.15594. URL <https://doi.org/10.48550/arXiv.2411.15594>.

Hu, Y., Li, T., Lu, Q., Shao, W., He, J., Qiao, Y., and Luo, P. OmniMedVQA: A new large-scale comprehensive evaluation benchmark for medical LVLM. In *IEEE/CVF Conference on Computer Vision and Pattern Recognition, CVPR 2024, Seattle, WA, USA, June 16-22, 2024*, pp. 22170–22183. IEEE, 2024. doi: 10.1109/CVPR52733.2024.02093. URL <https://doi.org/10.1109/CVPR52733.2024.02093>.

Johnson, A. E., Pollard, T. J., Berkowitz, S. J., Greenbaum, N. R., Lungren, M. P., Deng, C.-y., Mark, R. G., and Horng, S. MIMIC-CXR, a de-identified publicly available database of chest radiographs with free-text reports. *Scientific data*, 6(1):317, 2019.

Lau, J. J., Gayen, S., Ben Abacha, A., and Demner-Fushman, D. A dataset of clinically generated visual questions and answers about radiology images. *Scientific data*, 5(1):1–10, 2018.

Li, C., Wong, C., Zhang, S., Usuyama, N., Liu, H., Yang, J., Naumann, T., Poon, H., and Gao, J. LLaVA-Med: Training a large language-and-vision assistant for biomedicine in one day. In Oh, A., Naumann, T., Globerson, A., Saenko, K., Hardt, M., and Levine, S. (eds.), *Advances in Neural Information Processing Systems 36: Annual Conference on Neural Information Processing Systems 2023, NeurIPS 2023, New Orleans, LA, USA, December 10 - 16, 2023*, 2023.

Lin, C.-Y. Rouge: A package for automatic evaluation of summaries. In *Text summarization branches out*, pp. 74–81, 2004.

Liu, B., Zhan, L., Xu, L., Ma, L., Yang, Y., and Wu, X. Slake: A semantically-labeled knowledge-enhanced dataset for medical visual question answering. In *18th IEEE International Symposium on Biomedical Imaging, ISBI 2021, Nice, France, April 13-16, 2021*, pp. 1650–1654. IEEE, 2021. doi: 10.1109/ISBI48211.2021.9434010. URL <https://doi.org/10.1109/ISBI48211.2021.9434010>.

Liu, H., Li, C., Wu, Q., and Lee, Y. J. Visual instruction tuning. *CoRR*, abs/2304.08485, 2023. doi: 10.48550/ARXIV.2304.08485. URL <https://doi.org/10.48550/arXiv.2304.08485>.

Murphy, K. P. Reinforcement learning: An overview. *CoRR*, abs/2412.05265, 2024. doi: 10.48550/ARXIV.2412.05265. URL <https://doi.org/10.48550/arXiv.2412.05265>.

Pan, J., Liu, C., Wu, J., Liu, F., Zhu, J., Li, H. B., Chen, C., Ouyang, C., and Rueckert, D. MedVLM-R1: Incentivizing medical reasoning capability of vision-language models (VLMs) via reinforcement learning. In Gee, J. C., Alexander, D. C., Hong, J., Iglesias, J. E., Sudre, C. H., Venkataraman, A., Golland, P., Kim, J. H., and Park, J. (eds.), *Medical Image Computing and Computer Assisted Intervention - MICCAI 2025 - 28th International Conference, Daejeon, South Korea, September 23-27, 2025, Proceedings, Part VII*, volume 15966 of *Lecture Notes in Computer Science*, pp. 337–347. Springer, 2025. doi: 10.1007/978-3-032-04981-0_32. URL https://doi.org/10.1007/978-3-032-04981-0_32.

Schulman, J., Wolski, F., Dhariwal, P., Radford, A., and Klimov, O. Proximal policy optimization algorithms. *CoRR*, abs/1707.06347, 2017. URL <http://arxiv.org/abs/1707.06347>.

Sellergren, A., Kazemzadeh, S., Jaroensri, T., Kiraly, A. P., Traverse, M., Kohlberger, T., Xu, S., Jamil, F., Hughes, C., Lau, C., Chen, J., Mahvar, F., Yatziv, L., Chen, T. L., Sterling, B., Baby, S. A., Baby, S. M., Lai, J., Schmidgall, S., Yang, L., Chen, K., Bjornsson, P., Reddy, S., Brush, R., Philbrick, K., Asiedu, M., Mezerreg, I., Hu, H., Yang, H., Tiwari, R., Jansen, S., Singh, P., Liu, Y., Azizi, S., Kamath, A., Ferret, J., Pathak, S., Vieillard, N., Merhej, R., Perrin, S., Matejovicova, T., Ramé, A., Rivière, M., Rouillard, L., Mesnard, T., Cideron, G., Grill, J., Ramos, S., Yvinec, E., Casbon, M., Buchatskaya, E., Alayrac, J., Lepikhin, D., Feinberg, V., Borgeaud, S., Andreev, A., Hardin, C., Dadashi, R., Hussenot, L., Joulin, A., Bachem, O., Matias, Y., Chou, K., Hassidim, A., Goel, K., Farabet,

C., Barral, J. K., Warkentin, T., Shlens, J., Fleet, D. J., Cotruta, V., Sanseviero, O., Martins, G., Kirk, P., Rao, A., Shetty, S., Steiner, D. F., Kirmizibayrak, C., Pilgrim, R., Golden, D., and Yang, L. MedGemma technical report. *CoRR*, abs/2507.05201, 2025. doi: 10.48550/ARXIV.2507.05201. URL <https://doi.org/10.48550/arXiv.2507.05201>.

Shao, Z., Wang, P., Zhu, Q., Xu, R., Song, J., Zhang, M., Li, Y. K., Wu, Y., and Guo, D. Deepseekmath: Pushing the limits of mathematical reasoning in open language models. *CoRR*, abs/2402.03300, 2024. doi: 10.48550/ARXIV.2402.03300. URL <https://doi.org/10.48550/arXiv.2402.03300>.

Song, Y. and Kingma, D. P. How to train your energy-based models. *CoRR*, abs/2101.03288, 2021. URL <https://arxiv.org/abs/2101.03288>.

Team, L., Xu, W., Chan, H. P., Li, L., Aljunied, M., Yuan, R., Wang, J., Xiao, C., Chen, G., Liu, C., Li, Z., Sun, Y., Shen, J., Wang, C., Tan, J., Zhao, D., Xu, T., Zhang, H., and Rong, Y. Lingshu: A generalist foundation model for unified multimodal medical understanding and reasoning. *CoRR*, abs/2506.07044, 2025. doi: 10.48550/ARXIV.2506.07044. URL <https://doi.org/10.48550/arXiv.2506.07044>.

Vedantam, R., Zitnick, C. L., and Parikh, D. CIDEr: Consensus-based image description evaluation. In *IEEE Conference on Computer Vision and Pattern Recognition, CVPR 2015, Boston, MA, USA, June 7-12, 2015*, pp. 4566–4575. IEEE Computer Society, 2015. doi: 10.1109/CVPR.2015.7299087. URL <https://doi.org/10.1109/CVPR.2015.7299087>.

Wang, W., Gao, Z., Gu, L., Pu, H., Cui, L., Wei, X., Liu, Z., Jing, L., Ye, S., Shao, J., Wang, Z., Chen, Z., Zhang, H., Yang, G., Wang, H., Wei, Q., Yin, J., Li, W., Cui, E., Chen, G., Ding, Z., Tian, C., Wu, Z., Xie, J., Li, Z., Yang, B., Duan, Y., Wang, X., Hou, Z., Hao, H., Zhang, T., Li, S., Zhao, X., Duan, H., Deng, N., Fu, B., He, Y., Wang, Y., He, C., Shi, B., He, J., Xiong, Y., Lv, H., Wu, L., Shao, W., Zhang, K., Deng, H., Qi, B., Ge, J., Guo, Q., Zhang, W., Zhang, S., Cao, M., Lin, J., Tang, K., Gao, J., Huang, H., Gu, Y., Lyu, C., Tang, H., Wang, R., Lv, H., Ouyang, W., Wang, L., Dou, M., Zhu, X., Lu, T., Lin, D., Dai, J., Su, W., Zhou, B., Chen, K., Qiao, Y., Wang, W., and Luo, G. InternVL3.5: Advancing open-source multimodal models in versatility, reasoning, and efficiency. *CoRR*, abs/2508.18265, 2025a. doi: 10.48550/ARXIV.2508.18265. URL <https://doi.org/10.48550/arXiv.2508.18265>.

Wang, X., Yang, Z., Feng, C., Liang, Y., Zhou, Y., Liu, X., Zang, Z., Li, M., Lin, C., Lin, K., Li, L., Huang, F., and Wang, L. ViCrit: A verifiable reinforcement learning proxy task for visual perception in VLMs. *CoRR*, abs/2506.10128, 2025b. doi: 10.48550/ARXIV.2506.10128. URL <https://doi.org/10.48550/arXiv.2506.10128>.

Wang, Z., Zhu, J., Tang, B., Li, Z., Xiong, F., Yu, J., and Blaschko, M. B. Jigsaw-R1: A study of rule-based visual reinforcement learning with jigsaw puzzles. *Trans. Mach. Learn. Res.*, 2025, 2025c. URL <https://openreview.net/forum?id=XqQCsuyPve>.

Wasserthal, J., Breit, H.-C., Meyer, M. T., Pradella, M., Hinck, D., Sauter, A. W., Heye, T., Boll, D. T., Cyriac, J., Yang, S., et al. Totalsegmentator: robust segmentation of 104 anatomic structures in CT images. *Radiology: Artificial Intelligence*, 5(5):e230024, 2023.

Wei, J., Wang, X., Schuurmans, D., Bosma, M., Ichter, B., Xia, F., Chi, E. H., Le, Q. V., and Zhou, D. Chain-of-thought prompting elicits reasoning in large language models. In Koyejo, S., Mohamed, S., Agarwal, A., Belgrave, D., Cho, K., and Oh, A. (eds.), *Advances in Neural Information Processing Systems 35: Annual Conference on Neural Information Processing Systems 2022, NeurIPS 2022, New Orleans, LA, USA, November 28 - December 9, 2022*, 2022.

Wu, P., Zhang, Y., Diao, H., Li, B., Lu, L., and Liu, Z. Visual jigsaw post-training improves MLLMs. *CoRR*, abs/2509.25190, 2025. doi: 10.48550/ARXIV.2509.25190. URL <https://doi.org/10.48550/arXiv.2509.25190>.

Ye, J. and Tang, H. Multimodal large language models for medicine: A comprehensive survey. *CoRR*, abs/2504.21051, 2025. doi: 10.48550/ARXIV.2504.21051. URL <https://doi.org/10.48550/arXiv.2504.21051>.

Zhang, J., Liu, O., Yu, T., Hu, J., and Neiswanger, W. Euclid: Supercharging multimodal LLMs with synthetic high-fidelity visual descriptions. *CoRR*, abs/2412.08737, 2024. doi: 10.48550/ARXIV.2412.08737. URL <https://doi.org/10.48550/arXiv.2412.08737>.

Zhang, J., Khayatkhoei, M., Chhikara, P., and Ilievski, F. MLLMs know where to look: Training-free perception of small visual details with multimodal LLMs. In *The Thirteenth International Conference on Learning Representations, ICLR 2025, Singapore, April 24-28, 2025*. OpenReview.net, 2025. URL <https://openreview.net/forum?id=DgaY5mDdmT>.

Zhang, K., Yu, J., Yan, Z., Liu, Y., Adhikarla, E., Fu, S., Chen, X., Chen, C., Zhou, Y., Li, X., He, L., Davison, B. D., Li, Q., Chen, Y., Liu, H., and Sun, L. BiomedGPT:

A unified and generalist biomedical generative pre-trained transformer for vision, language, and multimodal tasks.
CoRR, abs/2305.17100, 2023a. doi: 10.48550/ARXIV.2305.17100. URL <https://doi.org/10.48550/arXiv.2305.17100>.

Zhang, S., Xu, Y., Usuyama, N., Xu, H., Bagga, J., Tinn, R., Preston, S., Rao, R., Wei, M., Valluri, N., et al. Biomed-clip: a multimodal biomedical foundation model pre-trained from fifteen million scientific image-text pairs.
arXiv preprint arXiv:2303.00915, 2023b.

Zhang, X., Wu, C., Zhao, Z., Lin, W., Zhang, Y., Wang, Y., and Xie, W. PMC-VQA: visual instruction tuning for medical visual question answering.
CoRR, abs/2305.10415, 2023c. doi: 10.48550/ARXIV.2305.10415. URL <https://doi.org/10.48550/arXiv.2305.10415>.

Zhu, J., Wang, W., Chen, Z., Liu, Z., Ye, S., Gu, L., Tian, H., Duan, Y., Su, W., Shao, J., Gao, Z., Cui, E., Wang, X., Cao, Y., Liu, Y., Wei, X., Zhang, H., Wang, H., Xu, W., Li, H., Wang, J., Deng, N., Li, S., He, Y., Jiang, T., Luo, J., Wang, Y., He, C., Shi, B., Zhang, X., Shao, W., He, J., Xiong, Y., Qu, W., Sun, P., Jiao, P., Lv, H., Wu, L., Zhang, K., Deng, H., Ge, J., Chen, K., Wang, L., Dou, M., Lu, L., Zhu, X., Lu, T., Lin, D., Qiao, Y., Dai, J., and Wang, W. InternVL3: Exploring advanced training and test-time recipes for open-source multimodal models.
CoRR, abs/2504.10479, 2025. doi: 10.48550/ARXIV.2504.10479. URL <https://doi.org/10.48550/arXiv.2504.10479>.

Zuo, Y., Qu, S., Li, Y., Chen, Z., Zhu, X., Hua, E., Zhang, K., Ding, N., and Zhou, B. MedXpertQA: Benchmarking expert-level medical reasoning and understanding. In *Forty-second International Conference on Machine Learning, ICML 2025, Vancouver, BC, Canada, July 13-19, 2025*. OpenReview.net, 2025. URL <https://openreview.net/forum?id=IyVcxU0RKI>.

A. Dataset Construction Details

In this appendix section, we provide a detailed breakdown of the data generation pipeline used to construct the dataset for Med-Scout training and the Med-Scout-Bench. Driven by the objective to cure geometric blindness without relying on expensive human annotations, our pipeline automatically extracts verifiable geometric supervision signals directly from raw medical images. We first elaborate on the composition and distribution of the 108,000-sample dataset, which spans diverse modalities including CT, MRI, and X-ray sourced from TotalSegmentor (Wasserthal et al., 2023; Akinci D'Antonoli et al., 2025) and MIMIC-CXR (Johnson et al., 2019). Subsequently, we describe the rigorous algorithmic protocols employed to synthesize the three geometric proxy tasks. Finally, we present the unified VQA instruction templates used to standardize these tasks for effective RL post-training.

A.1. Data Composition and Distribution Statistics

We primarily analyze the Med-Scout-Bench dataset. This is a specific test set of 10,800 examples designed to accurately measure geometric blindness. The rest of the data used for training and validation ($N = 97,200$) follows the same pattern, ensuring that the way the model is trained matches the way it is tested.

As shown in Figure 8, the benchmark follows two key distribution patterns:

- **Strict Modality Balance:** To avoid bias toward any specific imaging method, we ensure an equal distribution across the three main modalities. The benchmark is split evenly, with CT, MRI, and X-ray each making up about 33.3% of the data.
- **Task-Specific Distribution:** To ensure balanced training, we allocate sample sizes based on the difficulty of each task. We assign 1,800 samples to Task A (Hierarchical Scale Localization), as this fundamental spatial task requires less data to converge. The largest share (5,400 samples) goes to Task B (Topological Jigsaw Reconstruction); its complex anatomical puzzles require robust reasoning, necessitating more data. Finally, we dedicate 3,600 samples to Task C (Anomaly Consistency Detection), an intermediate amount sufficient for the model to learn to detect fine details and subtle anomalies.

A.2. Task-Specific Generation Protocols

A.2.1. HIERARCHICAL SCALE LOCALIZATION

This task is designed to compel the model to master absolute spatial grounding and multi-scale consistency. By forcing the model to map resized local patches back to their original global coordinates, we simulate a “zoom-in” clinical diagnostic process where a radiologist examines local details (e.g., a nodule) while maintaining awareness of its global position (e.g., upper right lung lobe). The generation process is formalized in Algorithm 1.

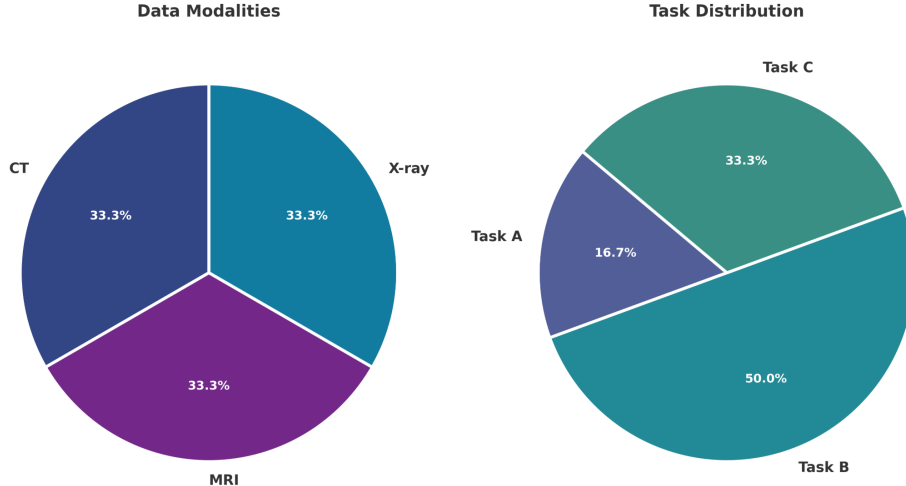


Figure 8. Data Statistics of Med-Scout-Bench. Left: The benchmark maintains a strictly balanced distribution across CT, MRI, and X-ray modalities to ensure unbiased geometric evaluation. Right: The benchmark is under task-specific distribution.

Scale Definitions and Sampling. We define two distinct scale levels to represent different granularities of anatomical detail:

- **Level 1 (Regional View):** The patch area covers 20% of the original image area ($A_{\text{patch}} \approx 0.2 \times A_{\text{total}}$).
- **Level 2 (Focal View):** The patch area covers 6.25% of the original image area ($A_{\text{patch}} \approx 0.0625 \times A_{\text{total}}$), corresponding to a $4 \times$ zoom relative to the original resolution.

For each training instance, we randomly extract $N = 3$ square patches. To ensure the patches contain meaningful anatomical information rather than non-informative background (e.g., black borders common in raw medical scans), the sampling of crop regions is strictly restricted to the valid central interval $[0.2, 0.8]$ of the image dimensions.

Input and Objectives. The input to the model consists of the original global image I_{global} followed by the three resized local patches $\{P_1, P_2, P_3\}$. All patches are resized to the dimensions of I_{global} . The model is prompted to perform two sub-tasks:

1. **Scale Classification:** Identify whether each patch belongs to Scale Level 1 or Level 2.
2. **Coordinate Regression:** Explicitly predict the normalized bounding box (x_1, y_1, x_2, y_2) of the patch in the original image frame.

Algorithm 1 Data Generation for Hierarchical Scale Localization

Require: Original Image $I \in \mathbb{R}^{H \times W}$

Require: Hyperparameters:

```

1:   Num Patches  $N \leftarrow 3$ 
2:   Scale Ratios  $\mathcal{S} \leftarrow \{0.20, 0.0625\}$  {Area ratios for Level 1 and Level 2}
3:   ROI Bounds  $[\alpha_{\min}, \alpha_{\max}] \leftarrow [0.2, 0.8]$  {Normalized valid center region}
4:   Target Size  $(H_{\text{out}}, W_{\text{out}}) \leftarrow (H, W)$  {Resize targets to original resolution}
Ensure: Resized Patches  $\mathcal{P}$ , Norm. Coordinates  $\mathcal{B}$ , Scale Labels  $\mathcal{L}$ 
5:   Initialize  $\mathcal{P} \leftarrow [], \mathcal{B} \leftarrow [], \mathcal{L} \leftarrow []$ 
6:   for  $k = 1$  to  $N$  do
7:     // Step 1: Determine Crop Size
8:     Sample ratio  $r \in \mathcal{S}$  uniformly
9:     Calculate square side length:  $l \leftarrow \sqrt{r \cdot H \cdot W}$ 
10:    // Step 2: Calculate Sampling Boundaries
11:    // Ensure crop is within ROI: start  $\geq \alpha_{\min}$ , end  $\leq \alpha_{\max}$ 
12:     $x_{\min} \leftarrow \alpha_{\min} \cdot W$ 
13:     $x_{\max} \leftarrow \alpha_{\max} \cdot W - l$ 
14:     $y_{\min} \leftarrow \alpha_{\min} \cdot H$ 
15:     $y_{\max} \leftarrow \alpha_{\max} \cdot H - l$ 
16:    // Step 3: Sample and Extract
17:    Sample top-left  $x \sim \text{Uniform}(x_{\min}, x_{\max})$ 
18:    Sample top-left  $y \sim \text{Uniform}(y_{\min}, y_{\max})$ 
19:     $\text{Patch}_{\text{raw}} \leftarrow I[y : y + l, x : x + l]$ 
20:    // Step 4: Resize and Normalize
21:     $\text{Patch}_{\text{resize}} \leftarrow \text{Resize}(\text{Patch}_{\text{raw}}, (H_{\text{out}}, W_{\text{out}}))$ 
22:     $\text{Box}_{\text{norm}} \leftarrow [x/W, y/H, (x + l)/W, (y + l)/H]$ 
23:    Append  $\text{Patch}_{\text{resize}}$  to  $\mathcal{P}$ ,  $\text{Box}_{\text{norm}}$  to  $\mathcal{B}$ ,  $r$  to  $\mathcal{L}$ 
24:   end for
25:   return  $\mathcal{P}, \mathcal{B}, \mathcal{L}$ 

```

A.2.2. TOPOLOGICAL JIGSAW RECONSTRUCTION

This task tests the model's ability to infer the overall anatomical structure from specific details. Unlike other jigsaw tasks that often use complex, many-piece grids, we use a simple 2×2 grid. This choice is essential for medical imaging:

- **Semantic Integrity:** A 2×2 grid ensures that each section contains recognizable anatomical features, such as a complete left lung or the clear shape of the pelvis.
- **Logical Deduction:** It shifts the reasoning burden from low-level pattern matching to high-level topological deduction (e.g., reasoning that the “heart” patch must be spatially adjacent to and above the “stomach” patch).

Generation Protocol. The image I is partitioned into four quadrants. We generate a random permutation σ of the index set $\{0, 1, 2, 3\}$, where indices correspond to the canonical reading order (top-left, top-right, bottom-left, bottom-right). The quadrants are rearranged according to σ to form the shuffled observation I_{shuffled} . The model is tasked with reconstructing the sequence of original indices. The detailed generation process is described in Algorithm 2.

Algorithm 2 Data Generation for Topological Jigsaw Reconstruction

Require: Original Image $I \in \mathbb{R}^{H \times W}$
Require: Hyperparameters:

- 1: Grid Dimension $G \leftarrow 2$ {Partitions image into 2×2 quadrants}
- 2: Patch Height $H_p \leftarrow H//G$
- 3: Patch Width $W_p \leftarrow W//G$
- 4: Canonical Indices $\mathcal{K} \leftarrow \{0, 1, 2, 3\}$ {Reading order: TL, TR, BL, BR}

Ensure: Shuffled Image I_{shuffled} , Target Sequence Y^*

- 5: // Step 1: Extract Canonical Patches
- 6: Define grid coordinates $C \leftarrow \{(0, 0), (0, W_p), (H_p, 0), (H_p, W_p)\}$
- 7: Initialize patch library $\mathcal{P}_{\text{lib}} \leftarrow []$
- 8: **for** $k \in \mathcal{K}$ **do**
- 9: $(y, x) \leftarrow C[k]$
- 10: Extract $P \leftarrow I[y : y + H_p, x : x + W_p]$
- 11: Append P to \mathcal{P}_{lib}
- 12: **end for**
- 13: // Step 2: Generate Permutation
- 14: Generate random permutation σ of \mathcal{K}
- 15: Initialize canvas I_{shuffled} of size $H \times W$
- 16: // Step 3: Reconstruct with Shuffled Order
- 17: **for** $i \in \mathcal{K}$ **do**
- 18: $idx_{\text{source}} \leftarrow \sigma[i]$ {Select which original patch goes to position i }
- 19: $(y_{\text{target}}, x_{\text{target}}) \leftarrow C[i]$ {Get coordinates for position i }
- 20: Place $\mathcal{P}_{\text{lib}}[idx_{\text{source}}]$ into I_{shuffled} at $(y_{\text{target}}, x_{\text{target}})$
- 21: **end for**
- 22: // Target is the permutation sequence defining the layout
- 23: $Y^* \leftarrow \sigma$
- 24: **return** I_{shuffled}, Y^*

A.2.3. ANOMALY CONSISTENCY DETECTION

This task trains the model to detect subtle anomalies and structural errors. We generate these examples using a “cut-paste” method: a section of the anatomy is replaced by a similar-looking, but incorrect, patch from a reference image (I_{ref}). To prevent the model from cheating by detecting sharp edges, we use Gaussian noise to blend the boundaries where the images meet.

Reference Image Selection (I_{ref}). To ensure the anomaly is non-trivial, we select I_{ref} based on modality-specific hardness:

- **Volumetric (CT/MRI):** I_{ref} is selected from a nearby slice ($z \pm 5$). This ensures the overall organ shape remains consistent, while introducing slight natural variations.
- **Planar (X-ray):** I_{ref} is the top-1 retrieval from the dataset via BiomedCLIP embedding similarity, ensuring semantic density consistency.

Generation Protocol. We partition the image into a 4×4 grid. The anomaly is injected into the central region defined by $\mathcal{C}_{\text{center}}$. Crucially, to mitigate the “sharp edge” artifact common in cut-paste augmentations, we add Gaussian noise to the boundary pixels of the pasted region. The detailed procedure and hyperparameters are formalized in Algorithm 3.

Algorithm 3 Data Generation for Anomaly Consistency Detection

Require: Target Image $I \in \mathbb{R}^{H \times W}$, Modality M , Database \mathcal{D}

Require: Hyperparameters:

- 1: Grid Dimension $G \leftarrow 4$
- 2: Patch Size $S \leftarrow (H/G, W/G)$
- 3: Center Indices $\mathcal{C}_{\text{center}} \leftarrow \{5, 6, 9, 10\}$ {Central 2×2 block in flattened index}
- 4: Noise Level $\sigma_{\text{noise}} \leftarrow 0.05$ {Std dev for boundary blending}
- 5: Boundary Width $\delta \leftarrow 2$ {Pixel width for noise injection}

Ensure: Anomalous Image I_{anom} , Anomaly Index k^*

- 6: // Step 1: Select Hard Negative Reference
- 7: **if** $M \in \{\text{CT, MRI}\}$ **then**
- 8: $I_{\text{ref}} \leftarrow \text{GetSlice}(I.\text{volume}, I.z \pm 1)$
- 9: **else**
- 10: $v_I \leftarrow \text{BioMedCLIP}(I)$
- 11: $I_{\text{ref}} \leftarrow \text{argmax}_{J \in \mathcal{D}, J \neq I} (\text{CosSim}(v_I, v_J))$
- 12: **end if**
- 13: // Step 2: Inject Anomaly with Edge Blending
- 14: Partition I_{ref} into grid \mathcal{P}_{ref}
- 15: Sample target index $k^* \sim \text{Uniform}(\mathcal{C}_{\text{center}})$
- 16: Extract foreign patch $P_{\text{foreign}} \leftarrow \mathcal{P}_{\text{ref}}[k^*]$
- 17: $I_{\text{anom}} \leftarrow I$
- 18: Paste P_{foreign} into I_{anom} at position k^*
- 19: // Step 3: Apply Boundary Noise
- 20: Get boundary region Ω of width δ around position k^*
- 21: Generate noise $\epsilon \sim \mathcal{N}(0, \sigma_{\text{noise}})$
- 22: $I_{\text{anom}}[\Omega] \leftarrow I_{\text{anom}}[\Omega] + \epsilon$
- 23: **return** I_{anom}, k^*

A.3. Unified VQA Instruction Formatting

To facilitate end-to-end training using a unified objective, we standardize all geometric proxy tasks into a consistent open-set VQA format. Instead of using task-specific heads, we formulate these tasks as natural language conversations.

As illustrated in Figure 9, each training instance is composed of three standardized components:

1. **Visual Input:** We use special tokens (e.g., <image>) to represent the medical scans. Note that for the *Hierarchical Scale Localization* task (Figure 9a), the input specifically supports multi-image sequences (Global View + Local Crops).
2. **User Prompt:** A structured instruction that clearly defines the geometric objective and constrains the output format.
3. **Target Response:** To support diverse inference strategies, we define two distinct output states:
 - **Direct Mode:** The model directly outputs the concise final answer (e.g., sequence indices or grid coordinates), focusing on strict format.
 - **Reasoning Mode:** The model first generates a CoT reasoning path enclosed in <think>...</think> tags to articulate geometric constraints before deriving the final answer enclosed in <answer>...</answer> tags.

Visual examples of the direct mode and the reasoning mode are provided in Figure 9 and Figure 10.

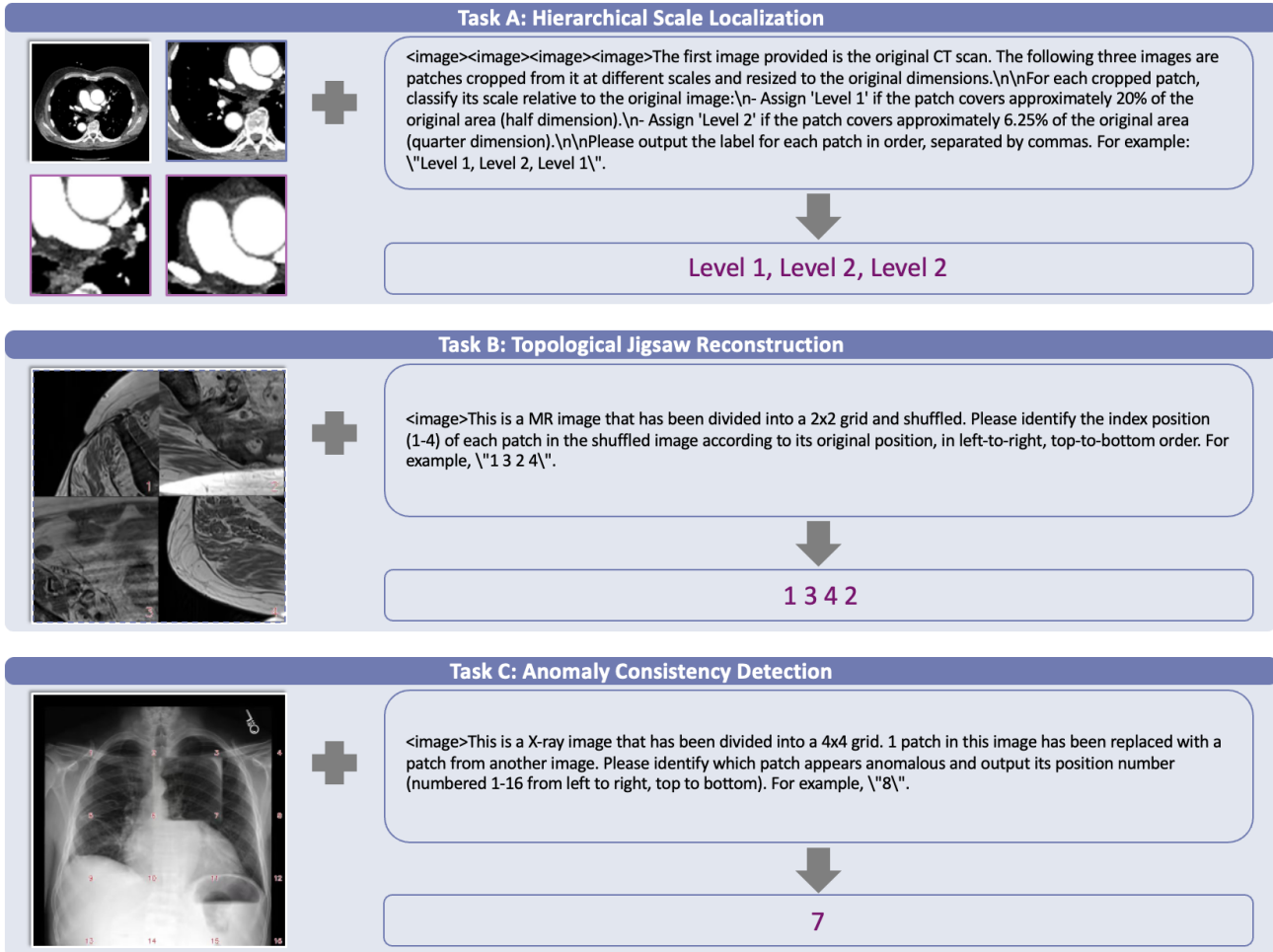


Figure 9. Unified VQA Instruction Examples of Direct Mode.

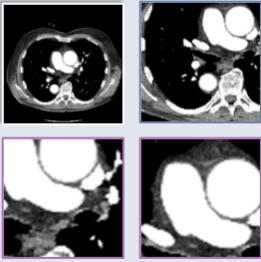
A.4. Med-Scout-Bench Evaluation Pipeline

To ensure consistent scoring across models with different styles, we use a standardized evaluation process as shown in Figure 11. Since MLLMs often provide detailed reasoning that makes simple text matching difficult, we use DeepSeek-V3.2 (DeepSeek-AI et al., 2025) to extract the conclusion from the raw output. These extracted answers are then automatically compared against the correct labels using a strict scoring script.



Figure 11. Evaluation pipeline on Med-Scout-Bench.

Task A: Hierarchical Scale Localization





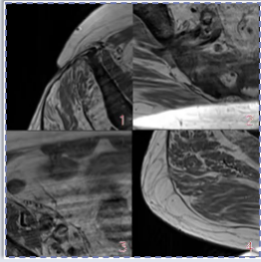
<image><image><image><image>The first image is the original CT scan with dimensions 512x512 pixels. The following three images are local patches cropped from it at different scales and resized to the original dimensions.\n\nIdentify the bounding box coordinates for each patch relative to the original image's coordinate system (where [0,0] is top-left). For each patch, provide the coordinates in the format: (x1, y1, x2, y2), where (x1, y1) is the top-left corner and (x2, y2) is the bottom-right corner.\n\nPlease output the pixel coordinates for each patch in order, separated by commas.\n\nPlease think step-by-step before providing your final answer. Put your reasoning in <think></think> tags, then provide the answer.\n\nFor example: '<think>reasoning process</think> <answer>(120, 85, 482, 447), (50, 200, 279, 429), (300, 150, 529, 379)</answer>'"

↓

<think>reasoning process</think>

<answer> Level 1, Level 2, Level 2 </answer>

Task B: Topological Jigsaw Reconstruction





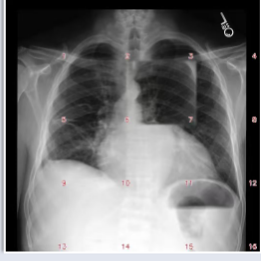
<image>This is a MR image that has been divided into a 2x2 grid and shuffled. Please identify the index position (1-4) of each patch in the shuffled image according to its original position, in left-to-right, top-to-bottom order.\n\nPlease think step-by-step before providing your final answer. Put your reasoning in <think></think> tags, then provide the answer.\n\nFor example, '<think>reasoning process</think> <answer>1 3 2 4</answer>'"

↓

<think>reasoning process</think>

<answer> 1 3 4 2 </answer>

Task C: Anomaly Consistency Detection





<image>This is a X-ray image that has been divided into a 4x4 grid. 1 patch in this image has been replaced with a patch from another image. The replaced patch is one of positions. Please identify which patch appears anomalous and output its position number (numbered 1-16 from left to right, top to bottom). \n\nPlease think step-by-step before providing your final answer. Put your reasoning in <think></think> tags, then provide the answer.\n\nFor example, '<think>reasoning process</think> <answer>8</answer>'"

↓

<think>reasoning process</think>

<answer> 7 </answer>

Figure 10. Unified VQA Instruction Examples of Reasoning Mode.

B. Training Implementation Details

B.1. Hyperparameters

We provide a comprehensive list of hyperparameters used during the Med-Scout RL post-training phase in Table 3. The training configuration is standardized across all backbone models to ensure fair comparison.

B.2. Training Costs

We provide a detailed breakdown of the computational costs associated with the geometry-aware post-training of different MLLM backbones. All training experiments were conducted on a single node equipped with $6 \times$ NVIDIA RTX PRO 6000

18

Table 3. Comprehensive list of hyperparameters for Med-Scout training. The configuration covers optimization, GRPO strategy, reward engineering, and system settings.

HYPERPARAMETER	VALUE	DESCRIPTION
<i>Optimization Configuration</i>		
OPTIMIZER	ADAMW	$\beta_1 = 0.9, \beta_2 = 0.95$
PEAK LEARNING RATE	1×10^{-6}	LOWER THAN SFT TO PREVENT COLLAPSE
LR SCHEDULER	COSINE DECAY	MINIMUM LR SET TO 1×10^{-7}
WARM-UP RATIO	0.01	LINEAR WARM-UP STRATEGY
WEIGHT DECAY	0.1	STANDARD REGULARIZATION
TRAINING STEPS	7200	TOTAL OPTIMIZATION UPDATES
<i>GRPO Strategy</i>		
GLOBAL BATCH SIZE	192	192 FOR ALL MODELS
GROUP SIZE (G)	8	NUMBER OF OUTPUTS SAMPLED PER PROMPT
KL COEFFICIENT (β)	0.04	PENALTY WEIGHT FOR POLICY DRIFT
CLIP RATIO (ϵ)	0.2	STANDARD PPO CLIPPING RANGE
<i>Reward Engineering</i>		
TOTAL MAX REWARD	2.0	SUM OF ACCURACY, FORMAT, AND REASONING REWARDS
ACCURACY CAP (\mathcal{R}_{ACC})	1.0	TASK-SPECIFIC GEOMETRIC PRECISION
FORMAT CAP (\mathcal{R}_{FMT})	0.5	SYNTAX COMPLIANCE REWARD
REASONING CAP ($\mathcal{R}_{\text{REASON}}$)	0.5	ACTIVE ONLY IN REASONING MODE (CoT)
ANOMALY TEMP (τ)	0.1	TEMPERATURE FOR DISTANCE-BASED REWARD
<i>System & Generation</i>		
MAX NEW TOKENS	1024	BUFFER FOR CoT REASONING TRACES
PRECISION	BF16	MIXED PRECISION TRAINING
HARDWARE	6× RTX PRO 6000	NVIDIA RTX PRO 6000 GPUs

Table 4. Training costs and configuration for different MLLM backbones.

MODEL	PARAMS	GLOBAL BATCH SIZE	STEPS	TOTAL GPU HOURS
QWEN3-VL-4B-INSTRUCT	4B	192	7,200	~ 530
QWEN3-VL-8B-INSTRUCT	8B	192	7,200	~ 801
HUATUOGPT-VISION-7B	7B	192	7,200	~ 783
LINGSHU-7B	7B	192	7,200	~ 767

GPUs (96GB VRAM each). The total training cost is primarily influenced by the model size and the configured global batch size. As detailed in the hyperparameters, we utilized a global batch size of 192 for all models to accommodate memory constraints during the high-throughput generation phase of GRPO. All models were trained for a total of 7,200 optimization steps.

Table 4 summarizes the GPU hours required for each model.

B.3. Reward Curves

To verify the stability and convergence of our geometry-aware post-training, we visualize the reward trajectories during the GRPO training phase. Figure 12 presents the comprehensive learning curves for both the Direct Mode and the Reasoning Mode across the four backbone models.

B.3.1. DIRECT MODE DYNAMICS

The first two panels of Figure 12 illustrate the training dynamics under the Direct Mode setting.

- **Dense Geometric Reward (\mathcal{R}_{acc}):** The *Direct - Accuracy* subplot depicts the steady improvement in geometric perception. We observe that general-domain models (Qwen3-VL series) achieve slightly higher accuracy (~ 0.84) compared to medical specialists (~ 0.72). This suggests that strong foundational vision-language capabilities are beneficial for solving complex spatial reasoning tasks.

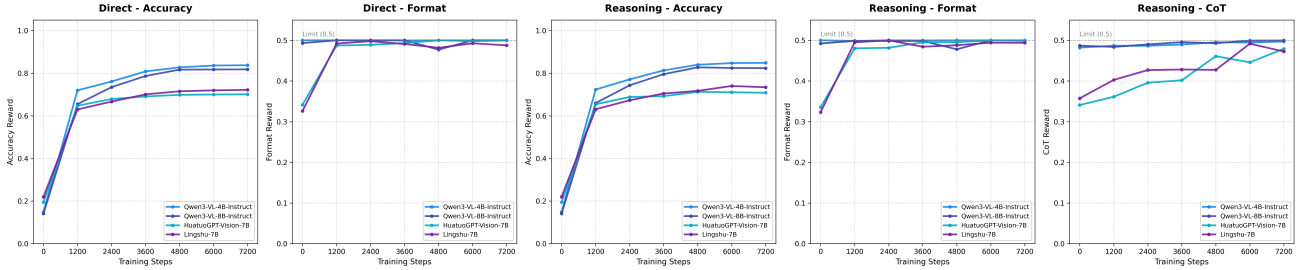


Figure 12. Training Reward Dynamics. The plots illustrate the optimization trajectories for Direct Mode (left two panels) and Reasoning Mode (right three panels). We report the Dense Geometric Rewards (\mathcal{R}_{acc}), Format Rewards (\mathcal{R}_{fmt}), and Reasoning Structure Rewards ($\mathcal{R}_{\text{reason}}$).

- **Format Reward (\mathcal{R}_{fmt}):** As shown in the *Direct - Format* subplot, all models rapidly master the requisite output format constraints (e.g., coordinate normalization, comma-separated lists). The format reward converges to the maximum value of 0.5 within the first 1,200 steps, indicating that the syntax of the geometric proxy tasks is easily learnable.

B.3.2. REASONING MODE DYNAMICS

In the Reasoning Mode, models are required to generate a CoT trace before the final answer. The last three panels of Figure 12 display the corresponding reward curves.

- **Dense Geometric Reward (\mathcal{R}_{acc}):** Compared to Direct Mode, the Reasoning Mode typically exhibits a slightly slower convergence rate initially due to the increased generation length and complexity. However, the final convergence values remain consistent with the Direct Mode, validating the robustness of the alignment strategy.
- **Format Reward (\mathcal{R}_{fmt}):** Similar to the Direct Mode, the format compliance in Reasoning Mode exhibits extremely rapid convergence. As shown in the *Reasoning - Format* subplot, all models quickly saturate at the maximum reward of 0.5, confirming that the increased sequence length from the reasoning process does not degrade the model's ability to adhere to syntactic instructions.
- **Reasoning Structure Reward ($\mathcal{R}_{\text{reason}}$):** As illustrated in the *Reasoning - CoT* subplot, the models effectively adapt to the `<think>...</think>` and `<answer>...</answer>` structure. Notably, while the general-domain Qwen3 models maintain high structural adherence from the start, the medical specialists (HuatuoGPT, Lingshu) show a distinct learning curve, requiring approximately 3,600 steps to converge to the maximum structural reward.

C. Extensive Experimental Results

C.1. Detailed Evaluation on Med-Scout-Bench

Due to space constraints in the main text, we focused on the aggregated geometric alignment scores. In this section, we provide a comprehensive performance breakdown for each backbone model across the three specific proxy tasks: Hierarchical Scale Localization ($\mathcal{T}_{\text{scale}}$), Topological Jigsaw Reconstruction ($\mathcal{T}_{\text{topo}}$), and Anomaly Consistency Detection ($\mathcal{T}_{\text{anom}}$).

The detailed numerical results are presented in Table 5. Beyond the performance gains, three notable patterns emerge from our findings:

- **General-Domain Models Learn Faster and Better:** General-purpose models (e.g., Qwen3-VL series) consistently outperform medical specialist models (e.g., Lingshu, HuatuoGPT) in learning geometric concepts. As shown in the reward curves and final scores, general models converge more rapidly and achieve significantly higher final accuracy. This suggests that a strong fundamental vision-language capability is more critical for grasping abstract spatial logic than domain-specific medical training.
- **Smaller Models Can Be More Efficient (4B vs. 8B):** Contrary to the scaling law expectation that “larger is better,” we observe that the Qwen3-VL-4B model learns faster and achieves higher geometric accuracy (Avg. 84.4) compared to its

larger 8B counterpart (Avg. 83.6). This indicates that for targeted geometric alignment, parameter efficiency and training dynamics may matter more than sheer model size.

- **Med-Scout Bridges the Gap with Proprietary Models:** In their base states, proprietary models like GPT-5 and Gemini-3-Flash significantly outperform open-source models (scoring 60% vs. 30%), likely due to their superior pre-training. However, after Med-Scout post-training, open-source models not only close this gap but easily surpass these closed-source leaders, with scores jumping to the 70%-90% range. This demonstrates that specific geometric supervision is highly effective at unlocking capabilities that even the strongest proprietary models lack.

Table 5. Performance evaluation on the Med-Scout-Bench. The table reports scores on three distinct subtasks and their average. All scores are scaled by a factor of 100 for better readability.

MODEL	MED-SCOUT-BENCH			
	TASK A	TASK B	TASK C	AVG.
<i>Proprietary Models</i>				
GPT-5	64.3	56.1	74.6	63.6
GEMINI-3-FLASH	67.0	58.8	76.7	66.1
<i>General-purpose MLLMs</i>				
INTERNVL3-8B	37.7	34.3	27.3	32.5
QWEN2.5-VL-3B-INSTRUCT	46.9	34.6	9.2	28.2
QWEN2.5-VL-7B-INSTRUCT	31.4	28.1	27.8	28.5
QWEN3-VL-4B-INSTRUCT	59.6	36.6	31.3	38.7
+ MED-SCOUT	94.4↑34.8	77.5↑40.9	89.8↑58.5	84.4↑45.7
QWEN3-VL-8B-INSTRUCT	41.0	34.7	46.4	39.7
+ MED-SCOUT	86.7↑45.7	78.1↑43.4	90.2↑43.8	83.6↑43.9
<i>Medical MLLMs</i>				
LLAVA-MED-7B	21.9	17.4	8.6	15.2
MEDGEMMA-4B-IT	46.4	33.5	29.0	34.1
HUATUOGPT-VISION-7B	60.7	33.7	28.0	36.3
+ MED-SCOUT	76.6↑15.9	79.3↑45.6	64.0↑36.0	73.8↑37.5
LINGSHU-7B	60.6	29.1	21.9	31.9
+ MED-SCOUT	78.9↑18.3	77.5↑48.4	60.0↑38.1	71.9↑40.0

C.2. Evaluation on Report Generation Tasks

The comprehensive results on the MIMIC-CXR and IU-Xray benchmarks are listed in Table 2. Beyond improving general-purpose models, Med-Scout proves effective at elevating already powerful domain specialists. Lingshu-7B, previously established as a SOTA medical MLLM, breaks through its performance ceiling after our alignment. It achieves a new SOTA CIDEr score on MIMIC-CXR, significantly outperforming proprietary commercial models. This indicates that our method provides a complementary geometric capability that is missing even in extensively trained medical models.

C.3. Task Difficulty Analysis

To investigate whether the complexity of the geometric proxy tasks contributes to the final post-training performance, we designed a controlled ablation study with three difficulty levels using Direct Mode. We constructed “Easy” and “Medium” variants of the training dataset by adjusting the complexity of the proxy tasks:

• Easy Variant:

- *Scale*: Single crop input ($N = 1$), removing the need for multi-scale comparative reasoning.
- *Topology*: Simple 1×2 grid shuffling, requiring only binary relative positioning.
- *Anomaly*: Coarse 2×2 grid (4 patches), making the foreign patch visually prominent.

• Medium Variant:

- *Scale*: Two crop inputs ($N = 2$), introducing limited multi-view context.

Table 6. Impact of Training Task Difficulty. We evaluate the Qwen3-VL-8B-Instruct model trained with datasets of varying geometric complexity (Easy, Medium, Hard) across radiological and general medical VQA benchmarks. Higher difficulty in proxy tasks consistently leads to superior generalization performance. The best results are highlighted.

TRAINING DIFFICULTY	RADIOLOGICAL VQA			GENERALIZATION		
	RAD-VQA	VQA-RAD	SLAKE	PMC-VQA	OMNIMEDVQA	MEDXPERTQA
<i>Baseline</i>						
QWEN3-VL-8B-INSTRUCT	41.6	63.2	69.6	43.9	42.9	30.4
<i>Med-Scout Variants</i>						
EASY DIFFICULTY	43.9↑2.3	65.1↑1.9	71.4↑1.8	44.2↑0.3	45.1↑2.2	30.5↑0.1
MEDIUM DIFFICULTY	44.8↑3.2	64.7↑1.5	71.8↑2.2	45.0↑1.1	45.7↑2.8	30.5↑0.1
HARD DIFFICULTY (OURS)	45.3↑3.7	65.8↑2.6	72.0↑2.4	45.5↑1.6	46.0↑3.1	30.8↑0.4
Δ	+0.5	+0.7	+0.2	+0.5	+0.3	+0.3

- *Topology*: 1×4 linear strip shuffling, increasing sequence length but lacking vertical spatial logic.
- *Anomaly*: Intermediate 4×2 grid (8 patches), requiring moderate attention granularity.

- **Hard Variant (Med-Scout Standard):**

- *Scale*: Three hierarchical crops ($N = 3$), forcing robust global-local mapping.
- *Topology*: 2×2 grid shuffling, necessitating 2D spatial reasoning (both horizontal and vertical).
- *Anomaly*: Fine-grained 4×4 grid (16 patches) with hard-negative mining, requiring pixel-level scrutiny.

Results. As shown in Table 6, while the difficulty level increases from “Easy” variants to the “Hard” (standard Med-Scout) setting, the model consistently achieves superior accuracy across external benchmarks. The “Hard” configuration, which enforces rigorous constraints, proved essential for achieving the best results. This confirms that high-complexity geometric objectives are necessary to prevent models from relying on superficial pattern matching, instead compelling them to master deep, pixel-level visual reasoning.

C.4. Impact of Proxy Task Types

To investigate the distinct contribution of each geometric proxy task to the overall performance, we conducted a comprehensive ablation study. Using Qwen3-VL-8B-Instruct as the backbone, we compared the baseline performance against variants trained with *Single Task Specialists* (using only one task type), *Leave-One-Out* Configurations (removing exactly one task type), and the full Med-Scout framework across six benchmarks.

The results are reported in Table 7. We observe that:

- **Every Proxy Task is Indispensable.** Comparing the full Med-Scout framework against the “Leave-One-Out” configurations reveals that removing any single geometric task leads to a consistent performance degradation across all benchmarks. This confirms that these three proxy tasks collectively establishing a holistic geometric perception that is superior to the sum of its parts.
- **Topology and Anomaly Tasks Drive Generalization.** The latter two tasks Topological Jigsaw Reconstruction (T_{topo}) and Anomaly Consistency Detection (T_{anom}) demonstrate a more critical impact on model performance and generalization. This suggests that the high-level logical deduction required for topology and the fine-grained scrutiny needed for anomaly detection are fundamental capabilities that generalize effectively to diverse medical imaging modalities.

C.5. Reward Mechanism Comparison

A critical component of the Med-Scout framework is the DGR mechanism, designed to overcome the sparsity of binary feedback in complex reasoning tasks. To quantify its impact, we compared our approach against a standard sparse reward baseline.

Table 7. Ablation Study of Proxy Task. We use Qwen3-VL-8B-Instruct as the backbone model to evaluate how different geometric tasks contribute to generalization performance across radiological and broad medical domains.

TRAINING CONFIGURATION	RADIOLOGICAL VQA			GENERALIZATION		
	RAD-VQA	VQA-RAD	SLAKE	PMC-VQA	OMNIMEDVQA	MEDXPERTQA
<i>Baseline</i>						
QWEN3-VL-8B-INSTRUCT	41.6	63.2	69.6	43.9	42.9	30.4
<i>Single Task Specialists</i>						
+ SCALE ONLY	42.9↑1.3	64.1↑0.9	70.3↑0.7	44.1↑0.2	43.9↑1.0	30.5↑0.1
+ TOPOLOGY ONLY	44.1↑2.5	64.9↑1.7	70.6↑1.0	44.8↑0.9	44.5↑1.6	30.7↑0.3
+ ANOMALY ONLY	44.6↑3.0	64.9↑1.7	71.0↑1.4	44.4↑0.5	44.7↑1.8	30.6↑0.2
<i>Leave-One-Out</i>						
+ MED-SCOUT (w/o SCALE)	44.9↑3.3	65.1↑1.9	71.4↑1.8	44.8↑0.9	45.3↑2.4	30.6↑0.2
+ MED-SCOUT (w/o TOPOLOGY)	44.7↑3.1	65.0↑1.8	71.1↑1.5	45.0↑1.1	45.5↑2.6	30.5↑0.1
+ MED-SCOUT (w/o ANOMALY)	44.8↑3.2	64.8↑1.6	70.8↑1.2	45.2↑1.3	45.4↑2.5	30.7↑0.3
+ MED-SCOUT (FULL)	45.3↑3.7	65.8↑2.6	72.0↑2.4	45.5↑1.6	46.0↑3.1	30.8↑0.4
Δ	+0.4	+0.7	+0.6	+0.3	+0.5	+0.1

Table 8. Impact of Reward Mechanism. Performance comparison between standard sparse reward and our dense geometric reward on six benchmarks. The dense mechanism provides granular feedback, leading to significantly better generalization.

REWARD STRATEGY	RADIOLOGICAL VQA			GENERALIZATION		
	RAD-VQA	VQA-RAD	SLAKE	PMC-VQA	OMNIMEDVQA	MEDXPERTQA
<i>Baseline</i>						
QWEN3-VL-8B-INSTRUCT	41.6	63.2	69.6	43.9	42.9	30.4
<i>+ Med-Scout</i>						
w/ SPARSE REWARD	44.7↑3.1	65.2↑2.0	71.3↑1.7	45.0↑1.1	45.8↑2.9	30.8↑0.4
w/ DGR (Ours)	45.3↑3.7	65.8↑2.6	72.0↑2.4	45.5↑1.6	46.0↑3.1	30.8↑0.4
Δ	+0.6	+0.6	+0.7	+0.5	+0.2	+0.0

- **Sparse Reward Setting:** The model receives a reward of $\mathcal{R} = 1$ only if the generated answer perfectly matches the ground truth (e.g., exact index sequence or coordinates within a strict threshold); otherwise, $\mathcal{R} = 0$.
- **Dense Reward Setting (Ours):** As detailed in Section 4.2, we utilize continuous metrics including IoU for bounding boxes, Euclidean distance decay for anomaly detection, and element-wise alignment for topological sequences.

Table 8 presents the comparison using the Qwen3-VL-8B-Instruct backbone. The results demonstrate that dense geometric reward provides a distinct optimization advantage over binary feedback. While the sparse reward setting already yields notable improvements over the baseline, the DGR mechanism consistently outperforms the sparse variant across all six benchmarks. As indicated by the Δ row, DGR achieves additional gains ranging from 0.2% to 0.7% on key datasets like VQA-RAD and SLAKE.

This confirms that the granular feedback provided by DGR is crucial for efficient RL post-training. Specifically, DGR awards partial credit for outputs such as “near-miss” scale predictions or approximate anomaly locations. In contrast, rigid pass/fail signals often fail to provide useful gradients for partially correct reasoning. Our DGR effectively guides the model to progressively refine its geometric understanding, which leads to superior generalization across both radiological and broad medical domains.

C.6. Comparison with Existing Proxy Tasks

We evaluate different proxy tasks using Qwen3-VL-4B-Instruct as the baseline. While Jigsaw-R1 (Wang et al., 2025c) and ViCrit (Wang et al., 2025b) introduce geometric constraints, they lack medical specificity and rely on sparse rewards. To ensure a fair comparison, we also restrict Med-Scout to use sparse rewards. As shown in Table 9, even under this constraint, Med-Scout achieves the highest accuracy, significantly outperforming general-domain methods. This confirms that domain-specific geometric alignment is essential for medical perception.

Table 9. Comparison with existing proxy tasks using Qwen3-VL-4B-Instruct. We evaluate Medical Design (Med.), Geometric Awareness (Geo.), and Reward Type. Even with sparse rewards, Med-Scout outperforms general-domain tasks. Best improvements are highlighted.

METHOD	MED.	GEO.	RADIOLOGICAL VQA			GENERALIZATION		
			RAD-VQA	VQA-RAD	SLAKE	PMC-VQA	OMNIMED	MEDXPERT
<i>Baseline</i>								
QWEN3-VL-4B-INSTRUCT	-	-	41.5	59.9	73.4	42.8	45.5	27.0
<i>Proxy Task Comparison</i>								
+ JIGSAW-R1	✗	✓	41.3 \downarrow 0.2	58.9 \downarrow 1.0	72.5 \downarrow 0.9	42.8 \uparrow 0.0	45.3 \downarrow 0.2	26.9 \downarrow 0.1
+ V1CRIT	✗	✗	41.0 \downarrow 0.5	59.2 \downarrow 0.7	72.8 \downarrow 0.6	43.0 \uparrow 0.2	45.5 \uparrow 0.0	26.8 \downarrow 0.2
+ MED-SCOUT (OURS)	✓	✓	45.7 \uparrow 4.2	62.9 \uparrow 3.0	75.6 \uparrow 2.2	45.1 \uparrow 2.3	48.8 \uparrow 3.3	27.7 \uparrow 0.7
Δ	-	-	+4.4	+3.7	+2.8	+2.1	+3.3	+0.8

Table 10. Comparison of SFT vs. RL on Med-Scout-Bench.

MODEL / METHOD	MED-SCOUT-BENCH			
	TASK A	TASK B	TASK C	AVG.
<i>Qwen3-VL-4B-Instruct</i>				
BASELINE	59.6	36.6	31.3	38.7
+ MED-SCOUT (SFT)	89.9 \uparrow 30.3	78.1 \uparrow 41.5	84.6 \uparrow 53.3	82.2 \uparrow 43.5
+ MED-SCOUT (RL)	94.4 \uparrow 34.8	77.5 \uparrow 40.9	89.8 \uparrow 58.5	84.4 \uparrow 45.7
Δ	+4.5	-0.6	+5.2	+2.2
<i>Qwen3-VL-8B-Instruct</i>				
BASELINE	41.0	34.7	46.4	39.7
+ MED-SCOUT (SFT)	85.1 \uparrow 44.1	76.9 \uparrow 42.2	88.7 \uparrow 42.3	82.2 \uparrow 42.5
+ MED-SCOUT (RL)	86.7 \uparrow 45.7	78.1 \uparrow 43.4	90.2 \uparrow 43.8	83.6 \uparrow 43.9
Δ	+1.6	+1.2	+1.5	+1.4
<i>HuatuoGPT-Vision-7B</i>				
BASELINE	60.7	33.7	28.0	36.3
+ MED-SCOUT (SFT)	79.2 \uparrow 18.5	79.3 \uparrow 45.6	65.1 \uparrow 37.1	74.6 \uparrow 38.3
+ MED-SCOUT (RL)	76.6 \uparrow 15.9	79.3 \uparrow 45.6	64.0 \uparrow 36.0	73.8 \uparrow 37.5
Δ	-2.6	+0.0	-1.1	-0.8
<i>Lingshu-7B</i>				
BASELINE	60.6	29.1	21.9	31.9
+ MED-SCOUT (SFT)	72.8 \uparrow 12.2	78.5 \uparrow 49.4	58.0 \uparrow 36.1	70.7 \uparrow 38.8
+ MED-SCOUT (RL)	78.9 \uparrow 18.3	77.5 \uparrow 48.4	60.0 \uparrow 38.1	71.9 \uparrow 40.0
Δ	+6.1	-1.0	+2.0	+1.2

C.7. SFT vs. RL

We observe a distinct contrast between internal alignment scores and external generalization capabilities:

- SFT Achieves Strong Performance on Internal Validation.** On the internal Med-Scout-Bench (Table 10), SFT demonstrates remarkable efficacy. It achieves performance levels comparable to or even surpassing the RL-tuned models. For example, HuatuoGPT-Vision-7B achieves an average score of 74.6% with SFT, compared to 73.8% with RL. This indicates that models can easily master the output syntax and specific data patterns of the proxy tasks through imitation.
- RL Enables True Generalization.** However, the apparent competence of SFT collapses on external benchmarks (Table 11). SFT variants exhibit negligible or even negative performance shifts. For instance, Qwen3-VL-8B-Instruct drops by 0.7% on Rad-VQA and 0.3% on MedXpertQA. This reveals that SFT merely overfits to the proxy task patterns without internalizing the underlying geometric reasoning. In contrast, RL achieves consistent gains across all external benchmarks. This confirms that exploration-driven optimization is essential for cultivating a generalized geometric perception that transfers beyond the training data.

Table 11. Comparison of SFT vs. RL on six external benchmarks.

MODEL / METHOD	RADIOLOGICAL VQA			GENERALIZATION		
	RAD-VQA	VQA-RAD	SLAKE	PMC-VQA	OMNIMEDVQA	MEDXPERTVQA
<i>Qwen3-VL-4B-Instruct</i>						
BASELINE	41.5	59.9	73.4	42.8	45.5	27.0
+ MED-SCOUT (SFT)	41.6 ^{↑0.1}	59.3 ^{↓0.6}	73.3 ^{↓0.1}	42.8 ^{↑0.0}	45.7 ^{↑0.2}	26.8 ^{↓0.2}
+ MED-SCOUT (RL)	45.7^{↑4.2}	62.9^{↑3.0}	75.6^{↑2.2}	45.1^{↑2.3}	48.8^{↑3.3}	27.7^{↑0.7}
Δ	+4.1	+3.6	+2.3	+2.3	+3.1	+0.9
<i>Qwen3-VL-8B-Instruct</i>						
BASELINE	41.6	63.2	69.6	43.9	42.9	30.4
+ MED-SCOUT (SFT)	40.9 ^{↓0.7}	63.1 ^{↓0.1}	69.8 ^{↑0.2}	44.5 ^{↑0.6}	42.7 ^{↓0.2}	30.1 ^{↓0.3}
+ MED-SCOUT (RL)	45.3^{↑3.7}	65.8^{↑2.6}	72.0^{↑2.4}	45.5^{↑1.6}	46.0^{↑3.1}	30.8^{↑0.4}
Δ	+4.4	+2.7	+2.2	+1.0	+3.3	+0.7
<i>HuatuoGPT-Vision-7B</i>						
BASELINE	48.8	67.0	67.8	53.0	75.0	22.4
+ MED-SCOUT (SFT)	48.5 ^{↓0.3}	67.1 ^{↑0.1}	68.0 ^{↑0.2}	52.6 ^{↓0.4}	75.1 ^{↑0.1}	22.1 ^{↓0.3}
+ MED-SCOUT (RL)	52.1^{↑3.3}	70.1^{↑3.1}	71.0^{↑3.2}	55.9^{↑2.9}	75.4^{↑0.4}	22.7^{↑0.3}
Δ	+3.6	+3.0	+3.0	+3.3	+0.3	+0.6
<i>Lingshu-7B</i>						
BASELINE	61.2	68.9	82.8	56.3	81.4	27.4
+ MED-SCOUT (SFT)	61.3 ^{↑0.1}	69.0 ^{↑0.1}	82.9 ^{↑0.1}	55.9 ^{↓0.4}	81.1 ^{↓0.3}	27.0 ^{↓0.4}
+ MED-SCOUT (RL)	64.0^{↑2.8}	71.0^{↑2.1}	83.0^{↑0.2}	57.4^{↑1.1}	81.9^{↑0.5}	28.0^{↑0.6}
Δ	+2.7	+2.0	+0.1	+1.5	+0.8	+1.0

D. Theoretical Analysis: Geometric Manifold Alignment

To rigorously justify that Med-Scout cures geometric blindness rather than merely overfitting to the proxy task templates, we analyze the learning process through the lens of Manifold Learning and Energy-Based Models (EBMs).

Formulation: Geometric Blindness as Manifold Deviation. Let the space of valid medical visual-text pairs lie on a high-dimensional manifold $\mathcal{M}_{geo} \subset \mathcal{X} \times \mathcal{Y}$. A pair (x, y) is geometrically valid if and only if it satisfies a set of intrinsic physical constraints \mathcal{C} (e.g., anatomical topology, scale consistency):

$$\mathcal{M}_{geo} = \{(x, y) \mid \mathcal{C}_{scale}(x, y) \wedge \mathcal{C}_{topo}(x, y) \wedge \mathcal{C}_{anom}(x, y) = \text{True}\} \quad (8)$$

Geometric Blindness occurs when an MLLM learns a strictly semantic distribution $P_\theta(y|x)$ that covers a broader, “hallucinated” manifold $\mathcal{M}_{halluc} \supset \mathcal{M}_{geo}$. Within \mathcal{M}_{halluc} , plausible but geometrically impossible descriptions (e.g., “liver on the left”) are assigned high probability (low energy), indistinguishable from factual descriptions.

Proxy Tasks as Manifold Constraints. Our three proxy tasks function not as simple Q&A pairs, but as constraint operators that explicitly penalize deviations from \mathcal{M}_{geo} . By optimizing the dense geometric reward, we are essentially minimizing the energy of the model distribution specifically on the manifold \mathcal{M}_{geo} . The objective of Med-Scout is to reshape the energy landscape $E(x, y) = -\log P_\theta(y|x)$ such that:

$$E(x, y_{halluc}) \gg E(x, y_{truth}), \quad \forall y_{halluc} \notin \mathcal{M}_{geo} \quad (9)$$

Specifically, the tasks enforce multi-scale correspondence (\mathcal{T}_{scale}), topological integrity (\mathcal{T}_{topo}), and fine-grained structural consistency (\mathcal{T}_{anom}).

Proof of True Grounding via Energy Landscapes. If the model were merely overfitting to the templates of the proxy tasks (e.g., memorizing specific grid indices), the energy landscape reshifting would be confined strictly to the subspace of those templates. However, our empirical analysis on natural language reports (Figure 6) proves this is not the case.

In Figure 6, we utilized a probe dataset of factual vs. counterfactual reports derived from MIMIC-CXR.

- **Baseline (Blindness):** The overlapping energy distributions (Gap ≈ 0.06) indicate that the baseline model treats the true manifold \mathcal{M}_{geo} and the hallucinated space \mathcal{M}_{halluc} as equiprobable.

- **Med-Scout (Aligned):** The emergence of a distinct energy barrier (Gap ≈ 0.69) on this natural language task serves as a theoretical certificate. It demonstrates that the constraints learned from the proxy tasks have successfully propagated to the general probability density function of the model.

This confirms that Med-Scout has successfully internalized the intrinsic boundaries of the medical geometric manifold \mathcal{M}_{geo} , rather than merely minimizing loss on a specific set of training artifacts. More energy gap results are shown in Figure 13.

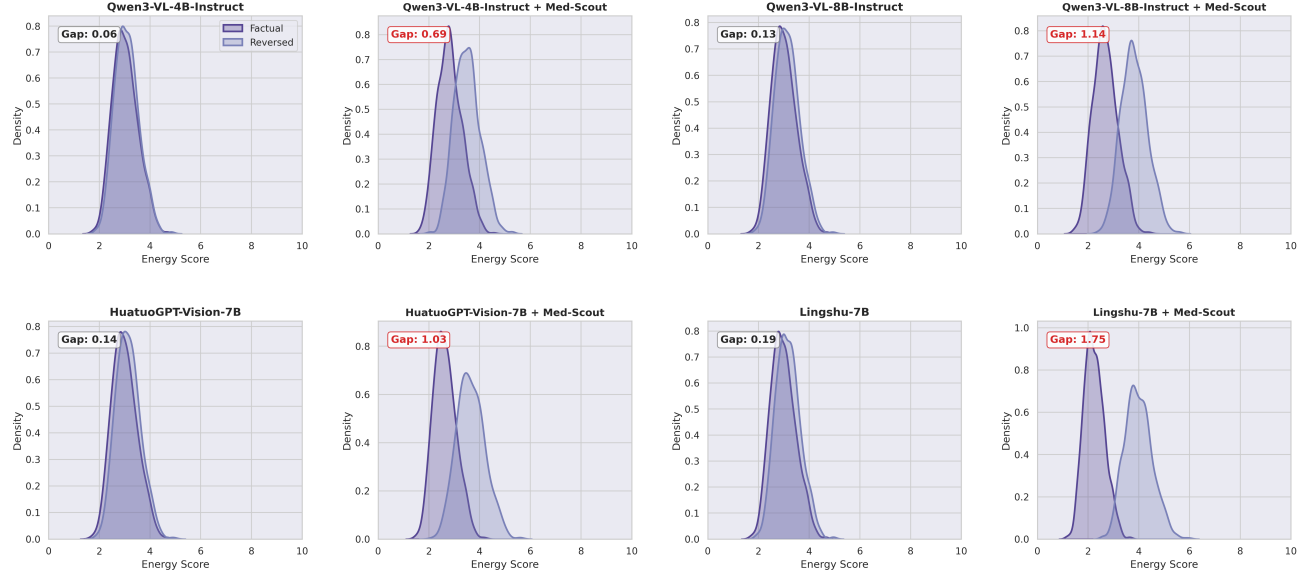


Figure 13. Comparison of energy score landscapes for four MLLMs. The panels illustrate the enhanced separation between factual and reversed samples achieved by Med-Scout, resulting in significantly wider energy gaps across all models.

E. Future Perspectives

While Med-Scout demonstrates significant improvements in curing geometric blindness, we acknowledge certain limitations in our current study that point towards promising directions for future research.

Validation on Model Scales. Our experiments were primarily conducted on MLLMs with parameters ranging from 3B to 8B (e.g., Qwen3-VL-4B/8B, Lingshu-7B). This choice was driven by computational resource constraints rather than inherent methodological limitations. The Med-Scout framework is designed to be model-size agnostic. We believe that the geometric alignment principles we proposed are equally applicable to larger-scale foundation models (e.g., 70B+ parameters). Applying Med-Scout to these larger models could potentially unlock even more robust geometric reasoning capabilities, as larger models typically possess stronger intrinsic world knowledge to support the alignment process.

Scope of Medical Modalities. Our current training data and Med-Scout-Bench focus on CT, MRI, and X-ray images. We selected these three modalities because they are the most representative forms of structural medical imaging with rigid geometric constraints. However, the core philosophy of Med-Scout, centered on *mining intrinsic visual logic from unlabeled data via proxy tasks*, holds promise for a much broader spectrum of medical imaging.

- **Generalizability to Other Domains:** The proxy task designs, such as hierarchical scale perception and anomaly consistency, can be adapted for Pathology (e.g., consistent reasoning across different magnifications in Whole Slide Images), Ultrasound (e.g., structural continuity detection), or other modalities such as Dermoscopy.
- **Unlabeled Data Potential:** By extending these ideas, we envision that Med-Scout can serve as a general paradigm to activate and enhance the fine-grained visual attention capabilities of MLLMs across diverse medical domains, leveraging the vast amounts of readily available unlabeled medical data.